

UNIVERSITY OF CALIFORNIA
Santa Barbara

Stochastic Modeling of System Function in a
Network of Biological Oscillators

A Dissertation submitted in partial satisfaction
of the requirements for the degree of

Doctor of Philosophy

in

Computer Science

by

Kirsten R. Meeker

Committee in Charge:

Linda R. Petzold, Chair

Francis J. Doyle III

John R. Gilbert

December 2014

The Dissertation of
Kirsten R. Meeker is approved:

Francis J. Doyle III

John R. Gilbert

Linda R. Petzold, Committee Chairperson

December 2014

Stochastic Modeling of System Function in a Network of Biological Oscillators

Copyright © 2014

by

Kirsten R. Meeker

To my parents, for passing on their sense of wonder and curiosity that enticed me to follow their path in science, and a sense of humor that kept me on it.

“A computer lets you make more mistakes faster than any invention in human history—with the possible exceptions of handguns and tequila.”
—Mitch Ratcliffe

Acknowledgements

I thank my committee for their time and dedication to educating students, and my advisor, Linda Petzold, for her sage advice and thorough reviews.

Curriculum Vitæ

Kirsten R. Meeker

Education

- | | |
|------|---|
| 2014 | Doctor of Philosophy in Computer Science, University of California, Santa Barbara (Expected). |
| 2004 | Master of Science in Computer Science, University of California, Santa Barbara |
| 1995 | Master of Science in Physics, California State University, Northridge |
| 1988 | Bachelor of Science in Physics, California State University, Northridge |

Professional Experience

- | | |
|-------------|--|
| 1989 – 2014 | Naval Air Warfare Center, Point Mugu, California |
| 1986 – 1988 | Research Assistant, California State University, Northridge. |

Awards

- | | |
|-----------|---|
| 2003-2004 | Naval Air Warfare Center Fellowship |
| 1996 | Ventura and Santa Barbara Counties Engineer of the Year |

Selected Publications

- Andrew C. Liu, David K. Welsh, Caroline H. Ko, Hien G. Tran, Eric E. Zhang, Aaron A. Priest, Ethan D. Buhr, Oded Singer, Kirsten Meeker, Inder M. Verma,

Francis J. Doyle III, Joseph S. Takahashi, and Steve A. Kay. Intercellular coupling confers robustness against mutations in the *scn* circadian clock network. *Cell*, 129(3):605–616, May 2007

- Neda Bagheri, Stephanie R. Taylor, Kirsten Meeker, Linda R. Petzold, and Francis J. Doyle. Synchrony and entrainment properties of robust circadian oscillators. *Journal of The Royal Society Interface*, 5(0):S17–S28, August 2008
- Richard Harang, Kirsten Meeker, Guillaume Bonnet, Francis J. Doyle III, and Linda R. Petzold. Period distribution in mammalian circadian neurons. In *Proceedings Foundations of Systems Biology in Engineering*, 2009
- Kirsten Meeker, Richard Harang, Alexis B. Webb, David K. Welsh, Francis J. Doyle, Guillaume Bonnet, Erik D. Herzog, and Linda R. Petzold. Wavelet measurement suggests cause of period instability in mammalian circadian neurons. *Journal of Biological Rhythms*, 26(4):353–362, 2011
- Sungwon An, Rich Harang, Kirsten Meeker, Daniel Granados-Fuentes, Connie A. Tsai, Cristina Mazuski, Jihee Kim, Francis J. Doyle, Linda R. Petzold, and Erik D. Herzog. A neuropeptide speeds circadian entrainment by reducing intercellular synchrony. *Proceedings of the National Academy of Sciences*, 2013

Abstract

Stochastic Modeling of System Function in a Network of Biological Oscillators

Kirsten R. Meeker

Many living organisms have evolved to anticipate daily circadian cycles and changing seasons of their environment. In mammals, the suprachiasmatic nucleus (SCN) of the hypothalamus, a brain region of about 20,000 neurons, serves as the master circadian clock coordinating timing throughout the body and entraining to daily external light cycles. The remarkable precision of the SCN clock relies on intercellular signaling. In its absence, each SCN neuron and the SCN as a whole have significantly less stable oscillations. Though there are candidate signaling neuropeptides and anatomical surveys of the SCN, it is still unknown how the SCN as a whole responds to changes in the environment and regulates function in the body. We model the unstable oscillations in individual cells by developing a stochastic model based on the cell clock's gene regulatory network, then investigate the intercellular signaling properties of the SCN to understand its behavior as a whole.

Though many existing deterministic models contain details of the gene regulation in the cell, their output has been compared to the behavior of the SCN as a

whole, rather than to individual cells. Characterizing properties of individual cells such as period, phase, and synchronization is challenging due to their non-linear and unstable oscillations. We developed a wavelet analysis method to characterize cell behavior in biological experiments and compare with stochastic cell models. This analysis led to an examination of how period distributions could be influenced by stochastic fluctuations in a nonlinear cell oscillator model, and a hypothesis that the poor or strong oscillators observed in biological experiments could be a stochastic oscillator operating near a bifurcation point, between non-oscillatory and oscillatory conditions.

It was observed in SCN tissue and in the SCN stochastic model that the oscillator is less likely to shift phase in response to a vasoactive intestinal polypeptide (VIP) dose at circadian time (CT4) than at other times. A reexamination of the behavior of the SCN as a whole, when modeled as linked stochastic oscillators, led to the hypothesis that the cells of the SCN synchronize to each other using a “phase tumbling” process. Our hypothesis is that the SCN synchronizes by its cells shifting with a wide phase distribution when they are perturbed at phases not near CT4. Rather than shifting in a deterministic manner, where all the cells stay synchronized and shift together to a new light schedule, they instead temporarily desynchronize then reorganize aligned to the new light/dark cycle. Within a few cycles the system can rapidly shift to a new light schedule. This

rapid re-entrainment to both new light/dark and temperature schedules was confirmed in mice by first desynchronizing the SCN using a neuropeptide that has been considered a synchronizing agent, vasoactive intestinal polypeptide, or by a brief bright light exposure before exposing the animals to a new shifted schedule.

Finally, since the behavior of the SCN as a whole may depend on the network topology of its intercellular connections, we applied an information theoretic measure to infer pairwise functional connections between neurons in the SCN. We first validated the method on several model networks. After inferring connection networks of three SCN's, we modeled those networks in our stochastic SCN model and confirmed that we could re-infer the bio-inspired networks. We found that the SCN, at least for these experimental samples, appears to have a small-world network topology and is scale-free. We hope that our results have helped to illuminate how stochastic fluctuations in the SCN system contribute to its behavior.

Contents

Acknowledgements	v
Curriculum Vitæ	vi
Abstract	viii
List of Figures	xii
List of Tables	xiii
1 Introduction	1
1.1 Mathematical Models	8
2 Background	21
2.1 Stochastic Simulation	21
2.2 Wavelets	24
3 Modeling Coupled Stochastic Mammalian Neurons	28
3.1 Simulation of a single cell	30
3.2 Simulation of a population	31
4 Unraveling the Source of Period-to-Period Variability in Cell Behavior	35
4.1 Experimental Procedure for Collecting Circadian SCN Data	37
4.2 Wavelet Analysis Reveals Non-Stationary Periods in PER2:LUC SCN Cells	38
4.3 Modeling Provides a Possible Mechanism	41

5	Phase Tumbling - A Theory of Entrainment	52
5.1	Experimental Results	55
5.1.1	VIP reduces the amplitude of circadian rhythms in the SCN by reducing synchrony	55
5.1.2	VIP reduces the synchrony of SCN populations	56
5.1.3	Constant light requires VIP to reduce circadian amplitude <i>in vivo</i>	57
5.2	Theory and Simulation	58
5.2.1	A computational model of circadian desynchronization pre- dicts faster entrainment	58
5.3	Experimental Validation of Phase Tumbling Hypothesis	61
5.3.1	VIP speeds photic entrainment <i>in vivo</i>	61
5.3.2	VIP speeds temperature entrainment of the SCN <i>in vitro</i>	62
6	Inference of Functional Network for Synchronization in the SCN	81
6.1	Inference Method	84
6.2	Validation with Model Circadian Networks	86
6.3	Biological Control and Connectivity Threshold	87
6.4	SCN Network Structure Results	89
6.4.1	SCN Coupling Displays a Small-World Architecture	89
7	Conclusions and Future Work	97
	Appendices	113
A	Leloup and Goldbeter 16-state Discrete Stochastic Model	114
B	11-state Circadian Model	120

List of Figures

1.1	Mammalian circadian system	2
1.2	Neuropeptide expression regions within the SCN	4
1.3	Mouse phase response curve (PRC)	7
1.4	3-state model of the circadian oscillator in a mammalian SCN neuron	9
1.5	16-state model of the circadian oscillator in a mammalian SCN neuron	14
1.6	Diagram of vasoactive intestinal polypeptide (VIP) intercellular signaling	16
2.1	Morlet wavelet function	26
2.2	PER2 expression recorded from three representative SCN cells	27
3.1	<i>Per</i> mRNA population as a function of basal transcription rate ν_{sP0} in uncoupled cells	33
3.2	<i>Per</i> mRNA in a stochastic simulation of coupled cells in a 5×5 grid	34
4.1	Magnitude heat maps resulting from Wavelet transform of dispersed cell PER2:LUC recordings from Herzog lab	44
4.2	Magnitude heat maps resulting from Wavelet transform of dispersed cell PER2:LUC recordings from Welsh lab	46
4.3	Histograms showing the period variability (standard deviation) of coupled and dispersed cells	47
4.4	Period distributions of dispersed and coupled SCN cells and stochastic model with parameter variations.	48
4.5	PER-CRY and CLOCK-BMAL1 feedback loop parameters and global scale factors that produce long periods	50
5.1	VIP dose-dependently reduces the amplitude of circadian rhythms in the SCN	65

5.2	VIP reduces the amplitude of PER2 rhythms after three washes	68
5.3	VIP dose-dependently reduces circadian synchrony among SCN cells	70
5.4	VIP mediates the amplitude reduction of locomotor rhythms by constant light	72
5.5	VIP accelerates circadian synchronization to an advanced schedule in vivo and in vitro	74
5.6	A computational model reveals that phase tumbling of circadian oscillators explains VIP-induced desynchrony and predicts that phase tumbling can speed entrainment	76
5.7	Stochastic model Phase Response Distribution (PRD) to VIP	78
5.8	Histograms showing the distribution of cells in response to light pulses at 24-h intervals computed from the PRD	80
6.1	Network inference results for three SCNs	93
6.2	Receiver Operator Characteristic (ROC) curves for model network validation	94
6.3	Area under the curve as a function of average node degree for model networks	94
6.4	Validation inference of connections between SCN samples	95
6.5	SCN node degree distribution is approximately scale-free	96

List of Tables

1.1	Parameter values for 3 state molecular clock model	11
1.2	Reaction steps in stochastic version of 3-state single cell model . .	13
4.1	Kullback-Leibler divergence of stochastic model and dispersed cell data.	45
6.1	SCN Network Characteristics	90
A.1	Reactions of discrete stochastic model based on 16 state Leloup & Goldbeter model with added CREB equation	114
A.2	Parameter values for 16 state molecular clock model	117
B.1	Ordinary differential equations comprising the 11-state circadian model.	120
B.2	Parameter descriptions for the 11-state circadian ODE model. . .	122

Chapter 1

Introduction

The adaptation of organisms to their environment has long been of interest to biologists. An important adaptation is the ability to anticipate daily circadian cycles and changing seasons. This improves an organism's survival by enabling it to predict food availability, predator activity, and weather conditions. Seasonal changes in day-length provide an environmental cue for seasonal migration, hibernation, and reproduction.

Internal clocks in both plants and animals, which allow them to keep time in the absence of environmental cues, were discovered by observing organism behavior. In 1729, Jean-Jacques d'Ortous de Mairan, a French chronobiologist, demonstrated the existence of an endogenous clock in a plant by showing that the opening and closing of its leaves continued in constant darkness [31]. In 1918,

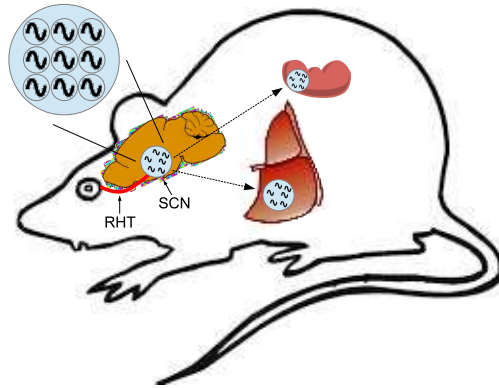


Figure 1.1: The multi-cellular master circadian clock in the SCN receives light input via the retinohypothalamic tract (RHT) allowing it to entrain to the environment. The SCN then passes that information on to peripheral oscillators in other organs [88].

J.S. Szymanski showed that animals can maintain circadian rhythms in behavior in the absence of light or temperature cues [1]. An endogenous clock is a key adaptation in both plants and animals that gives them the ability to anticipate daily and seasonal cycles.

In mammals, the suprachiasmatic nucleus (SCN) of the hypothalamus, a brain region of about 20,000 neurons, serves as the master circadian clock coordinating timing throughout the body and entraining to daily external light cycles (Fig. 1.1) [88]. Each neuron by itself oscillates with less precision than the SCN as a whole. Experiments in which cell-to-cell signaling between SCN neurons is disrupted by

physical separation of the cells [116, 51] or by blocking neuropeptide mediated signaling [11] show that the remarkable precision of the circadian clock at the level of the organism relies on this intercellular signaling. In the absence of cell-to-cell signaling, each SCN neuron and the SCN as a whole have significantly less stable oscillations. This has been measured in PER2:LUC bioluminescence recordings, firing rate recordings, and animal behavioral data.

The loss of synchrony with physical separation of cells was demonstrated by dispersing them at low densities *in vitro*. [116, 51] Synchrony is restored in high-density dispersals. [12] Cutting the SCN into separate regions [123] showed that the dorsal (upper) third was unable to retain synchrony while the ventral (lower) third remained synchronized. Both sections had roughly the same number of cells. Since anatomical projections from the ventral to dorsal sections are more dense than the reverse [4] this is interpreted to mean that the ventral section drives synchrony in the dorsal section.

Desynchrony can also be produced by chemically canceling the effect of neurotransmitters between SCN neurons. One method is to use tetrodotoxin (TTX) to block sodium-dependent action potentials.[12, 54] Two candidates for synchronizing neurotransmitters are gamma-aminobutyric acid (GABA) and vasoactive intestinal polypeptide (VIP). GABA is produced by most of the cells in the SCN and its receptors are also found throughout the SCN (Fig. 1.2). In addition, it

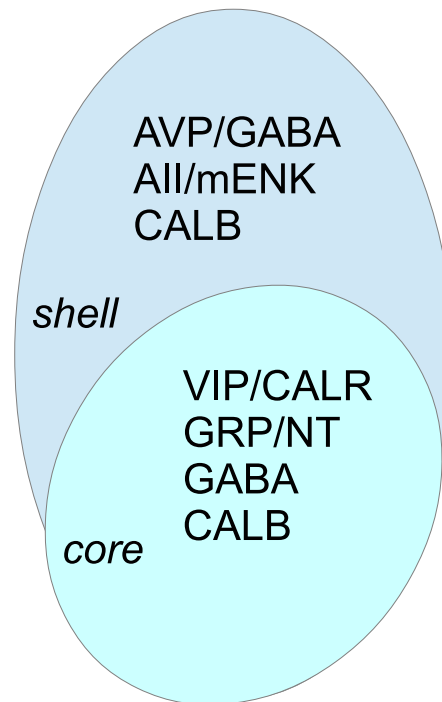


Figure 1.2: Neuropeptide expression regions within the SCN. Vasoactive intestinal polypeptide (VIP), gastrin releasing peptide (GRP), neurotensin (NT), and calretinin (CALR) are expressed in the core. Arginine vasopressin (AVP), met-enkephalin (mENK), and angiotensin II (AII) are expressed in the shell. GABA and calbindin (CALB) are expressed throughout the mouse SCN [4]. In humans the areas expressing VIP and AVP overlap more [90].

has a circadian expression profile. Together these properties meet the criteria for a candidate synchronizing neurotransmitter. Application of a GABA_A agonist to SCN slices produced desynchrony similar to cutting the dorsal and ventral regions apart. Again, the dorsal portion lost synchrony while the ventral portion retained it.[7]

VIP is produced by only about 15% of SCN cells, which are located in the ventral SCN and receive input from the retinohypothalamic tract (RHT). The VIP receptor, VPAC2, (encoded by *Vipr2* gene) is expressed by about half of the ventral cells and almost all of the dorsal cells. VIP^{-/-} and *Vipr2*^{-/-} (knockout) mutant SCN lost cell synchrony. Rhythmicity in individual cells decreased from 70% of wild-type to about 30% of mutant neurons. Other neuropeptides such as gastrin-releasing peptide (GRP), neurotensin (NT), and prokinecton 2 (PK2) also meet the candidate criteria and warrant further investigation.[82, 72, 76]

In the absence of light input, the endogenous circadian clock will free-run at its own intrinsic period which can be different from 24 hrs. In the presence of light-dark cycles, SCN gene expression and neuron firing rates entrain, matching phase with the external light-dark cycle. Humans experience the symptoms of jet lag, when this entrainment is temporarily disturbed by rapid travel to a new time zone. There is evidence that seasonal variations in day length are encoded in the

SCN by a distribution of the phase of entrainment across the cells of the SCN, with some cells matching dawn and others dusk [23].

Circadian oscillators exhibit a phase-dependent resetting property in which the magnitude and direction of a phase shift response depends on the circadian time at which a stimulus occurs. This property can be characterized by a phase response curve. Figure 1.3 shows an example mouse phase response to 15-minute light pulses. Typically phase response curves have been measured for either animal behavior or the SCN as a whole, in which case they represent the mean response of a population of cells. All circadian systems respond with a phase delay in early subjective night and a phase advance in late subjective night, and some exhibit a “dead” zone as shown in Figure 1.3. Subjective night is defined as the segment of a circadian cycle during the free-running state that corresponds to the dark segment during entrainment by a light-dark cycle. Circadian time is a standard of time based on the free-running period. By convention, the onset of activity of diurnal organisms defines circadian time zero (CT 0). The onset of activity of nocturnal organisms defines circadian time twelve (CT 12).[87]

The PRC for brief light pulses has been a successful model for explaining the entrainment of organisms exposed to less-than full photo-periods. However, the magnitude and shape of the PRC changes (in a non-linear manner) with the duration and strength of the perturbing light pulse. Consequently, the brief

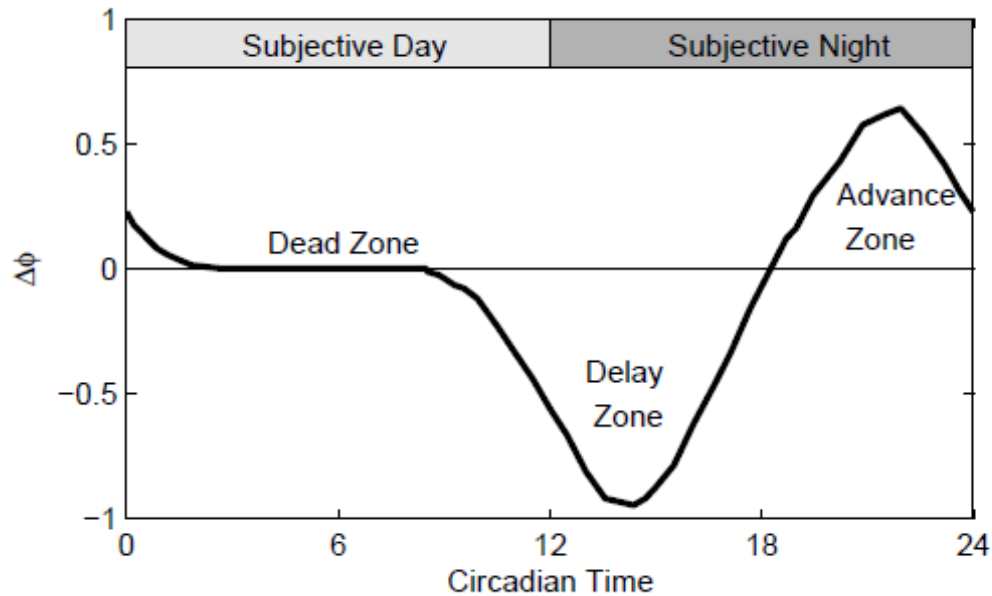


Figure 1.3: Mouse phase response curve (PRC). This PRC for 15 minute light pulses has a phase delay in early subjective night of up to 1 hour and a phase advance in late subjective night of up to 0.6 hours. It has a dead zone, where there is no phase shift, during the subjective day from CT2 to CT8. Night and day are subjective here because the PRC is measured in all dark conditions after the animal is pre-conditioned by exposure to light/dark cycles. Figure reproduced with permission from [101].

light-pulse PRC is not as good at predicting the response of organisms to full photo-periods.[60] The period (x-axis) and function of the PRC may be changed by exposure to a complete photo-period. ([26], [83]) VanderLeest et al. [106] recorded differences in the PRC of mice exposed to long vs. short photo-periods, observing large phase delays in mice exposed to short photo-periods and small delays in mice exposed to long photo-periods. These phase shift responses were measured in terms of wheel running behavior. Examination of SCN rhythms revealed high amplitudes in slices from short days and low amplitudes in slices from long days. This led to the proposal that synchronization among SCN neurons enhances its phase shifting capacity.[106]

1.1 Mathematical Models

The details of how circadian clock oscillations in organisms are produced began to be revealed in the early 1970s when Ron Konopka and Seymour Benzer isolated the first clock mutant in *Drosophila* and mapped the “period” gene.[64] The first ‘clock gene’ (*clock*) in mammals was discovered in 1994 by Joseph Takahashi.[109] Since then many more circadian genes have been identified, and many models of the gene regulatory network: the biochemical reactions within the cell that produce its circadian rhythm, have been built. In 2004, a PERIOD2::LUCIFERASE

Gene symbols are italicized and protein symbols use all uppercase letters

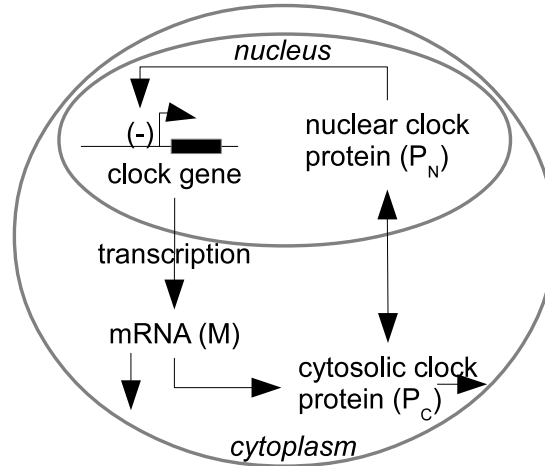


Figure 1.4: 3-state model of the circadian oscillator in a mammalian SCN neuron [44]. Cytosolic clock protein P_C enters the nucleus P_N where it represses transcription of its clock gene to mRNA M .

fusion protein was created by Takahashi's lab and used for the first time as a real-time reporter of the circadian clock in mice.[124] Since this first demonstration, PER2:LUC has been used under many different experimental conditions to measure circadian rhythms in individual cells and the SCN as a whole, providing the data needed to build a model of the SCN to understand how synchronization and entrainment work.

A minimal molecular clock model (Fig. 1.4) is described by three equations (1.1-1.3) governing messenger ribonucleic acid (mRNA), cytosolic and nuclear clock proteins.[44] This simple model can reproduce sustained oscillations in all dark (circadian biologists refer to this as dark:dark) conditions by a repressive

feedback loop in the gene regulation. Cytosolic clock protein P_C enters the nucleus P_N where it represses transcription of its clock gene to mRNA M . With the addition of light input (by temporarily increasing the mRNA transcription rate parameter ν_s , Table 1.1) this model can also reproduce a phase shift in response to light pulses and entrainment to light-dark cycles. Gonze and Goldbeter [44] also demonstrated the synchronization of five stochastic oscillators using five unique nuclei with a shared cytoplasm, a form of global coupling possible in the fungus *Neurospora* which can have several nuclei in a single cell.

$$\frac{dM}{dt} = \nu_s \frac{K_l^n}{K_l^n + P_N^n} - \nu_m \frac{M}{K_m + M} \quad (1.1)$$

$$\frac{dP_C}{dt} = k_s M - \nu_d \frac{P_C}{K_d + P_C} - k_1 P_C + k_2 P_N \quad (1.2)$$

$$\frac{dP_N}{dt} = k_1 P_C - k_2 P_N \quad (1.3)$$

The transcription rate of mRNA M from the clock gene is governed by two terms describing production and degradation of mRNA (Eqn. 1.1). The production term is a Hill equation for describing cooperative binding of a ligand to a macromolecule. The cooperative binding is modeled by a rate that scales non-linearly with the ligand concentration. In this case the Hill coefficient n is positive, which means that binding of a ligand molecule increases the affinity of the next ligand molecule for the macromolecule. Gonze and Golbeter [44] point out that

Table 1.1: Parameter values for 3 state molecular clock model

Parameter	Value
ν_s	0.82 nMh ⁻¹
K_l	1 nM
n	4
ν_m	0.42 nMh ⁻¹
K_m	0.50 nM
k_s	0.42 h ⁻¹
ν_d	1.2 nMh ⁻¹
K_d	0.13 nM
k_1	0.42 nMh ⁻¹
k_2	0.50 nMh ⁻¹

oscillations will still occur if the cooperativity is reduced to one, but that a larger value expands the region of parameter space over which the model will sustain oscillations. The degradation term is assumed to follow Michaelis-Menten enzymatic kinetics, where M is the substrate, and K_m is the substrate concentration at which the reaction rate is half of its maximum ν_m .

The rate of change of cytosolic protein P_C (Eqn. 1.2) is governed by the transport of mRNA into the cytoplasm (first term), a Michaelis-Menten degradation term (second), and terms (third and fourth) describing the transport of protein balanced between the cytoplasm and nucleus. The rate of change of nucleic protein P_N (Eqn. 1.3) is described by the same terms (third and fourth) in the cytosolic protein equation, which are just the balance of protein between the two cell regions.

A stochastic version of the single cell model is produced by converting each term in the differential equation model into a reaction step (see Table 1.2). Each reaction step is assigned a probability equal to the deterministic reaction rate scaled by a volume parameter Ω which determines the number of molecules in the system. Gonze and Golbeter [44] produced a stochastic version of this simple molecular clock model by connecting species concentrations in the deterministic model to species populations in the stochastic model.

Table 1.2: Reaction steps in stochastic version of single cell model. The volume parameter Ω determines the number of molecules and degree of stochasticity. The deterministic limit corresponds to $\Omega \rightarrow \infty$.

No.	Reaction	Transition rate
1	$\rightarrow M$	$w_1 = \nu_s \Omega \frac{K_l \Omega^n}{K_l \Omega^n + P_N^n}$
2	$M \rightarrow$	$w_2 = \nu_m \Omega \frac{M}{K_m \Omega + M}$
3	$\rightarrow P_C$	$w_3 = k_s M$
4	$P_C \rightarrow$	$w_4 = \nu_d \Omega \frac{P_C}{K_d \Omega + P_C}$
5	$P_C \rightarrow P_N$	$w_5 = k_1 P_C$
6	$P_N \rightarrow P_C$	$w_6 = k_2 P_N$

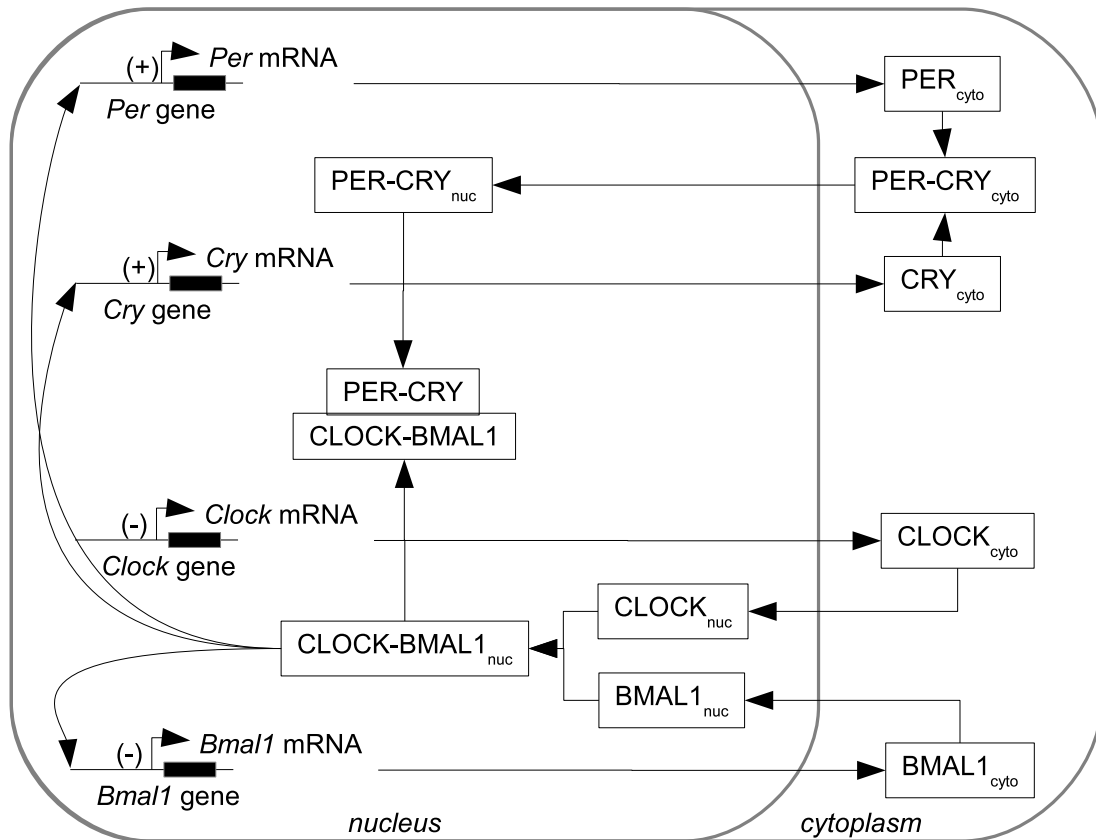


Figure 1.5: 16-state model of the circadian oscillator in a mammalian SCN neuron [66]. Oscillations derive from regulatory feedback loops involving *period*, *cryptochrome*, *Bmal1*, and *clock* gene and protein components. Some proteins, such as *clock*, are thought to be constitutively expressed, and are not included as independent states of the mathematical ordinary differential equation model. Additional protein phosphorylation and degradation reactions are not shown in this diagram.

The 16-state molecular clock model (Fig. 1.5) due to Leloup and Goldbeter [66] adds many details missing from the simple 3-state model. It expands the number of genes from one generic to five specific: Period (*Per*), Cryptochrome (*Cry*), *Bmal1*, *Clock*, and *Rev-Erb* alpha, adds phosphorylated states for many of the proteins corresponding to these genes, and adds protein dimer complexes PER-CRY and CLOCK-BMAL. Tables A.1–A.2 located in Appendix A provide the reaction probabilities and parameter values of the stochastic version which was developed as part of this thesis project.

To et al. [104] developed a model of intercellular synchronization using the 16-state clock model by adding equations describing vasoactive intestinal polypeptide (VIP) signaling between cells (Fig. 1.6). The effect of a cell’s VIP release on surrounding cells was assumed to be inversely proportional to the distance between them on a two-dimensional grid. To et al. [104] simulated a 20 x 20 grid of VIP-coupled cells, demonstrating their ability to synchronize in constant darkness, entrain to periodic light input through VIP, and desynchronize in constant light/VIP.

The intercellular coupling [104] shown in Figure 1.6 is defined by the following equations. The extracellular VIP produced by a cell i is given by

$$\rho_i(t) = a\Omega \frac{M_{P,i}(t)}{M_{P,i}(t) + b\Omega}, \quad (1.4)$$

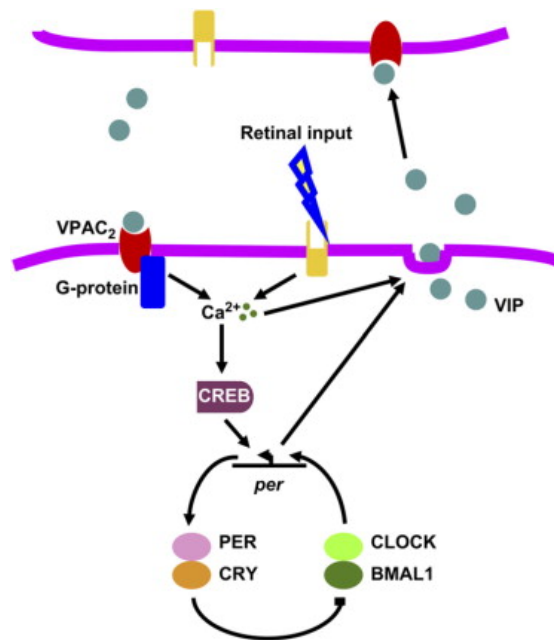


Figure 1.6: Diagram of vasoactive intestinal polypeptide (VIP) intercellular signaling [104]. VIP is shown being released from one cell membrane and traveling to attach to the G-protein coupled receptor $VPAC_2$ on another cell's membrane. This increases the Calcium level in the cell, which activates CREB. At a particular phase in the circadian cycle, CREB induces *Per* transcription.

where Ω is the stochastic volume parameter, M_p is the *Per* mRNA, a is the maximum VIP release, and b is the saturation constant. The VIP observed by cell i due to cell j is given by

$$\gamma_i(t) = \frac{1}{\epsilon} \sum_{j=1}^N \alpha_{ij} \rho_j(t) \quad (1.5)$$

$$\epsilon = \frac{1}{N} \sum_{i=1}^N \sum_{j=1}^N \alpha_{ij}, \quad (1.6)$$

where the weighting factor α_{ij} is the reciprocal of the distance between cells i and j , and ϵ is the mean weight across the population. The extent of receptor saturation on a scale of 0 to 1 ($\beta = 1$ at complete saturation) is modeled as

$$\beta = \frac{\gamma}{K_D \Omega + \gamma}. \quad (1.7)$$

The equilibrium dissociation constant is K_D . The cytosolic calcium balance is given by

$$k\Omega C a_{Cytosol}^{2+} = \nu_0 \Omega + \nu_1 \Omega \beta, \quad (1.8)$$

which equates the cytosolic efflux (left-hand side) to the sum of the influx of extracellular Ca^{2+} (ν_0), input due to VIP signaling, and light input, where γ ranges from 0 (dark) to 1 (maximum light). The effect of Ca^{2+} on CREB is assumed to follow Michaelis-Menten kinetics

$$\nu_K = V_{MK} \Omega \frac{C a_{Cytosol}^{2+}}{K_a + C a_{Cytosol}^{2+}}, \quad (1.9)$$

where K_a is the substrate concentration at which the reaction rate is half of its maximum V_{MK} . The extent of CREB activation λ is modeled as

$$\lambda = \frac{CB_T CB^*}{K_C \Omega + CB_T CB^*}, \quad (1.10)$$

where CB_T is the total amount of CREB, CB^* is the fraction of CREB in phosphorylated form, and K_C is the dissociation constant. The maximum *Per* transcription rate ν_{sP} is given by

$$\nu_{sP} = \nu_{sP0} \Omega + C_T \lambda, \quad (1.11)$$

where ν_{sP0} is the basal transcription rate and C_T is the scaled maximum effect of the CREB-binding element on the *Per* gene.

To et al. [104] introduced heterogeneity into the model cell population by using Gaussian distributions for some of the parameters in the core clock model. They found a reduction in the precision of synchronization of the population as the standard deviation of the parameter distribution was increased. This deterministic modeling approach for creating a population distribution is different from a stochastic model that exhibits a population distribution due to fluctuations (beside circadian oscillations) in individual cell biochemistry over time. Both genetic heterogeneity (as modeled in To et al.) and stochasticity are present in the true biological system, however the assumption that the two sources of population distribution can be interchanged (ergodicity) is not necessarily a valid one.[55]

Deterministic circadian gene regulation models have been used to model synchronization and entrainment in the SCN [104]. However, these models are unable to reproduce the variability observed in PER2:LUC recordings of individual cells. The variability observed in cell recordings points to the importance of including stochastic fluctuations in a model of the SCN.

The objective of this project was to build a stochastic model of the SCN which reproduces cell and system level behavior observed in PER2:LUC recordings, and to use it to understand the interplay between intrinsic noise in cell gene regulation, the intercellular communication required for cell synchronization, and the SCN's (cell population) response to environmental signals.

The remainder of this thesis is organized as follows. Chapter 2 reviews classes of chemical reaction system models and the stochastic simulation algorithm, and provides background on wavelets and the analysis of nonstationary data using the Morlet wavelet. Chapter 3 presents a stochastic model of the SCN and its synchronization properties, depending on the level of stochasticity and intercellular connection networks. In Chapter 4 we compare recordings of circadian neurons and stochastic models using wavelets to measure instantaneous phase and period variability, and investigate the model parameter space capable of reproducing the biological results. In Chapter 5 the phase response distribution of cells in the SCN and 'phase tumbling' as a conceptual model for synchronization and entrainment

of cells in the SCN is presented. Finally, in Chapter 6 we develop a methodology for inference of a functional intercellular network in the SCN using an information theoretic measure, and present and discuss the results.

Chapter 2

Background

2.1 Stochastic Simulation

Until recently, most models of the SCN have been continuous and deterministic. They assume the presence of large numbers of molecules and that the reactions are far from any point of chemical instability. Population distributions have been created by assigning parameter values over some distribution, so that all of the cells are not identical. This approach is unable to reproduce fluctuations in individual cell dynamics. A discrete stochastic model produces fluctuations in individual cell dynamics and population distributions based on the underlying physics of the chemical reactions, and may predict outcomes different from continuous deterministic models.

There are three classes of models of chemical reaction systems: continuous deterministic, continuous stochastic, and discrete stochastic. Continuous deterministic models are described with rate equations that are ordinary differential equations. These models assume that the numbers of molecules are large enough that fluctuations can be ignored. Continuous stochastic models are described by Langevin or stochastic differential equations, which consist of ordinary differential equations with an additional Gaussian noise term. They are valid in the regime where a time step can be found that is small enough that reaction propensities (the probability for a given reaction to fire during the next infinitesimal time interval dt) do not change much and are large enough that each reaction in the system occurs more than once [41]. Discrete stochastic models use an exact description in which each reaction fires according to the probability given by its propensity.

The Stochastic Simulation Algorithm (SSA) due to Gillespie [40] computes the trajectory of chemical species in a reaction system from the reaction probability density function, $P(\tau, j)$. $P(\tau, j)$ is defined by the expression $P(\tau, j)d\tau$, which is the joint probability that the next reaction will occur in the time interval $(t + \tau, t + \tau + d\tau)$, and will be an R_j reaction of M possible reactions R_1, \dots, R_M . The probability that reaction R_j occurs in the next infinitesimal time interval dt is

$$P(R_j, dt) = a_j(X(t))dt, \tag{2.1}$$

Paul Langevin (23 January 1872 – 19 December 1946) was a prominent French physicist who developed an equation in statistical physics to describe Brownian motion.

where a_j is the propensity function of R_j , and $X(t) = X_1(t), \dots, X_N(t)$ is the current state of the system. Given S_1, \dots, S_N chemical species, $X_i(t)$ is the number of S_i molecules at time t .

At each update of the algorithm, two random numbers r_1 and r_2 are drawn from a uniform distribution $U(0, 1)$ and used to compute the time τ when the next reaction R_j occurs. The time to the next reaction τ is chosen by sampling from an exponential distribution

$$\tau = \frac{1}{a_0(X(t))} \ln \left(\frac{1}{r_1} \right). \quad (2.2)$$

The reaction R_j is selected by choosing the smallest integer j satisfying the relation

$$\sum_{j'=1}^j a_{j'}(x) > r_2 a_0(x). \quad (2.3)$$

The sum of all the reaction propensities

$$a_0(X(t)) = \sum_{i=1}^M a_i(X(t)) \quad (2.4)$$

is used to normalize the total probability to one. Once the reaction is selected, the state $X(t)$ is updated by the change in numbers of molecules ν_j of the reacting species.

$$X = X + \nu_j \quad (2.5)$$

The basic discrete stochastic model assumes that the system is well stirred, i.e. that a given molecule is just as likely to be in one spatial location as another.

Other assumptions are that the system is at a constant temperature and the volume Ω is fixed.

2.2 Wavelets

Measuring the period and phase of a stochastic oscillator can be challenging due to its non-stationary nature. In this case we need to measure the time-varying period and phase, a time–frequency tiling [20] of the data. The Fourier transform is commonly used to convert a signal to the frequency domain and identify periodic components. It does not work well by itself on non-stationary signals. The windowed Fourier transform uses a fixed sized window which, depending on the frequencies contained in the signal being analyzed, will give either good time resolution or good frequency resolution but not both simultaneously. Wavelet transforms were created in part for multiresolution analysis and provide good time resolution for high frequencies and good frequency resolution for low frequencies [27]. Thus they are better suited for measuring signals containing a wide range of frequencies. Since the stochastic oscillator is driven by molecular events, it inherently has multiple time scales, and one of our questions was whether it also has multiple frequencies.

The Morlet (or Gabor) wavelet function is given by

$$\Psi(t) = \pi^{-1/4} e^{i\omega_0 t} e^{-t^2/2}, \quad (2.6)$$

which is a Fourier function windowed by a Gaussian. The frequency of the wavelet, ω_0 , is rescaled to examine all potential frequencies. Scaled and translated wavelets are generated using the scale factors a and b and the equation

$$\Psi_{a,b}(t) = \frac{1}{\sqrt{a}} \Psi\left(\frac{t-b}{a}\right). \quad (2.7)$$

The continuous wavelet transform (CWT) of a signal f in L1 can be defined by the inner product

$$W_{a,b} = \langle f(t), \Psi_{a,b}(t) \rangle. \quad (2.8)$$

The continuous wavelet transform (CWT) of a signal generates an array of complex numbers. Taking the magnitude provides a measure of the strength of a given frequency at a given point in time. If there is a single dominant frequency present at each point in time it can be extracted from the magnitude heat map to determine the instantaneous period and phase of the oscillator (Fig. 2.2).

WAVOS (Wavelet Analysis and Visualization of Oscillatory Signals), a MATLAB toolbox developed by Richard Harang, was used for analysis in this thesis [49]. In addition to computing the period of the oscillator over time, WAVOS also provides functions which use the CWT to estimate the instantaneous phase, and the synchronization index of oscillators. Its discrete (Daubechies) wavelet

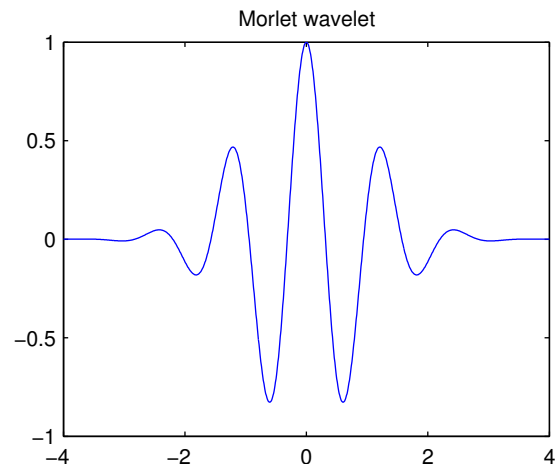


Figure 2.1: Morlet wavelet function.

transform functions have better time localization properties than the CWT and can be used to remove transients in the data.

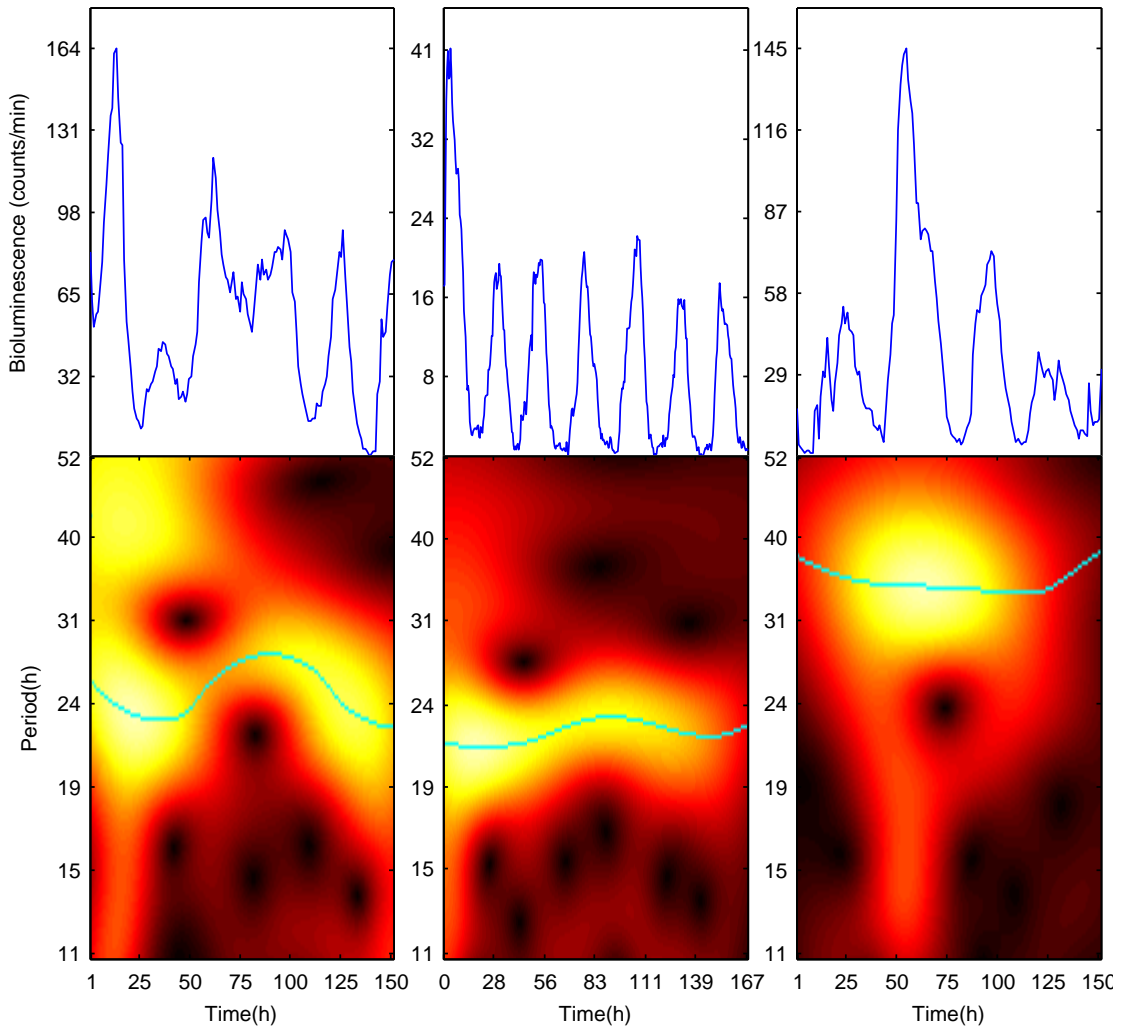


Figure 2.2: PER2 expression recorded from three representative SCN cells over 7 days showing examples of cells with unstable (A), stable (B), or absent (C) circadian periods. The heatmap plots from each cell show the amplitude of the Continuous Wavelet Transform and the maximum amplitude at each moment (ridge highlighted in green). Note that this ridge plot changes little in the more stable circadian cell, gradually drifts between 23 and 38 hours in the unstable cell, and is consistently infradian (longer than circadian) in the final plot.

Chapter 3

Modeling Coupled Stochastic

Mammalian Neurons

In mammals, the circadian master clock resides in the suprachiasmatic nucleus (SCN), located in the hypothalamus [88]. It is a network of multiple autonomous noisy oscillators, which communicate via neuropeptides to synchronize and form a coherent oscillator [53] [68]. This coherent oscillator then coordinates the timing of daily behaviours, such as the sleep/wake cycle. Biological experiments, however, demonstrate that uncoupled neurons in the SCN are either damped or sloppy oscillators [12]. Thus, coupling in the SCN causes a collection of stochastic, unreliable oscillators to form a robust oscillator that can be reliably reset. To unravel the design principles behind this remarkable behaviour, mathemat-

ical models must incorporate the stochastic properties of the single cell, while coupling the population of cells through biophysical components. A putative coupling agent is vasoactive intestinal (neuro)peptide (VIP) [53], whose inter-cellular concentration levels peak during the subjective day. It has been demonstrated that controlled VIP pulses cause phase shifts similar to those resulting from light pulses [82], suggesting that the VIP signal and target are similar to those of light and may be modeled correspondingly. The target of VIP signaling is therefore assumed to be *Per* transcription.

Experimental data demonstrate that isolated (uncoupled) neurons exhibit both a broad distribution of periods and temporal (cycle-to-cycle) variability [53]. Hao et al. [47] and To et al. [104] postulated mechanisms through which VIP signals are received by a cell via signal cascades, culminating in the modulation of parameter associated with *Per* transcription. Using an ODE model, To et al. [104] incorporate this coupling mechanism into a population of non-identical cells, each of which is based on the gene regulatory network model of Leloup & Goldbeter [66]. They simulate scenarios with no coupling (the cells drift out of phase) and with coupling (the cells form a coherent oscillator), demonstrating that their mechanism is capable of creating the spontaneous synchronization seen in experimental data. Likewise, their simulations show a broad distribution of periods across cells. However, because they use a deterministic model, they do not repro-

duce cycle-to-cycle variation. We develop a discrete stochastic model based on that in To et al. [104] incorporating intrinsic noise, and consequently temporal variability.

We simulate this model in a two-dimensional grid of 25 SCN neurons using the software package STOCHKIT2 [92] based on the stochastic simulation algorithm (SSA) [40] [42]. Successful synchronization of 25 coupled cells validates the mechanism in the presence of noise.

The work described in this Chapter was published in Neda Bagheri, Stephanie R. Taylor, Kirsten Meeker, Linda R. Petzold, and Francis J. Doyle. Synchrony and entrainment properties of robust circadian oscillators. *Journal of The Royal Society Interface*, 5(0):S17–S28, August 2008. Our contribution was the stochastic simulation results.

3.1 Simulation of a single cell

The introduction of noise alters the behaviour of single cells such that additional tuning of the model is required to achieve synchrony. In particular, because

Gillespie [41] offers an explanation of the conditions under which Langevin and deterministic chemical kinetics approximations are valid. This is usually the case when populations of all the reactant species are sufficiently large. This condition may not hold in the biological system being modelled, and is not the case in the predictions of the Leloup & Goldbeter deterministic model (some species concentrations approach zero during low points in the oscillatory cycle); therefore a deterministic approximation using ODEs may not be completely adequate for our purposes.

VIP signalling ultimately manifests as modulation of the rate of *Per* transcription, special attention must be paid to the levels of *Per* mRNA and its rate of transcription, $\nu_{sP}(t)$. The basal rate ν_{sP0} characterizes the behaviour of an isolated cell: *Per* mRNA oscillations are damped when $\nu_{sP0} < 1.2$ and sustained when $\nu_{sP0} \geq 1.2$ (Fig. 3.1). Figure 6 in Leloup & Goldbeter [67] shows the period versus ν_{sP0} , which peaks at $\nu_{sP0} = 1.5$ with a period of 23.8 hours. The depletion or accumulation of *Per* mRNA that occurs when ν_{sP0} is below 1.2 indicates that the balance is upset between the transcription rate and the combination of the transport (from nucleus to cytoplasm) and degradation. For the coupled population to exhibit synchrony, we have observed that the median value of $\nu_{sP}(t)$ must stay within the range that produces oscillations in an individual cell. Thus to achieve synchrony, the basal transcription rate ν_{sP0} has been set to 1.5 for the coupling topology and volume used in this work. At this basal transcription rate, all isolated cells are oscillators.

3.2 Simulation of a population

Simulation of a 5×5 grid of cells shows that the VIP coupling mechanism is capable of achieving synchrony (Fig. 3.2) between stochastic cells exhibiting temporal variability in period and amplitude. To measure the phase coherence of

the cells in a simulation, we use the radius $r(t)$ of the complex order parameter [100], computed according to

$$r(t) = \frac{1}{N} \sum_{j=1}^N e^{i(\theta_j - \Psi)}, \quad (3.1)$$

where N is the number of cells; θ_j is the phase of the j th oscillator; and $\Psi(t)$ is the average phase. If the oscillators are in phase, $r(t) \approx 1$. Here the mean $r(t)$ across 10 simulations begins at 0.2–0.3 with uniform random initial phase and increases to 0.8 in 14 cycles when coupled. These data demonstrate the effective response of intercellular signalling that gives rise to phase synchrony. As in Gonze et al. [45], proximity to the bifurcation point $\nu_{sP0} = 1.06$ [67] in the deterministic ODE model predicts oscillatory behaviour in the stochastic simulation based on the same cell model. Unlike the results in Gonze et al. [43], synchronization of the 5×5 grid of cells does not occur when the coupling parameter is below the bifurcation point where individual cells are damped oscillators. This is due to both the nature of the individual cell model and the properties of the coupling signal, which are dependent on the grid connectivity, size and coupling strength. The range of ν_{sP0} , which permits synchronization using mean-field coupling, appears to be bounded on the low end by the bifurcation point. For this choice of connectivity and coupling strength, ν_{sP0} has a fairly narrow range that will allow synchronization. Presumably this is due to the independent ν_{sP0} signals overpowering the common coupling signals [58]. In Bernard et al. [18], this self-feedback is modeled as an

autocrine signal that is scaled with the same coupling strength as signals from other cells. As the coupling strength is increased, the autocrine signal is also increased. This is analogous to increasing ν_{sP_0} in this model to produce rhythmic cells. Maywood et al. [71] observed that in an intact SCN the loss of VIP coupling had the effect of suppressing rhythmicity in many cells and loss of synchrony in the cells that retained rhythmicity.

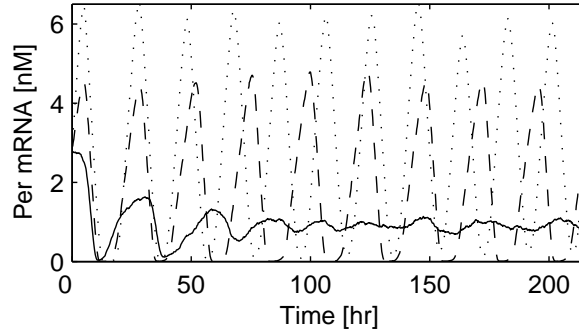
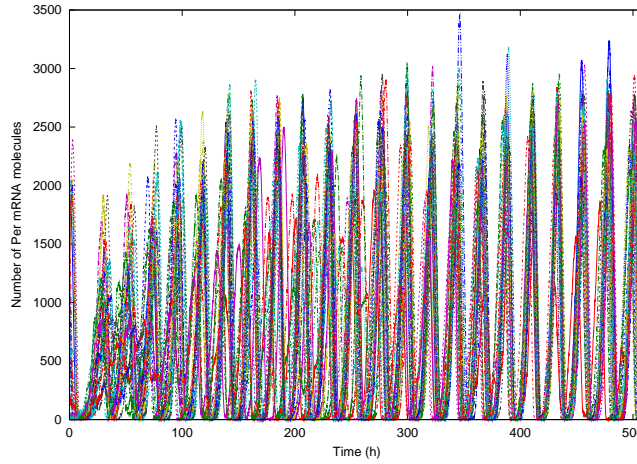
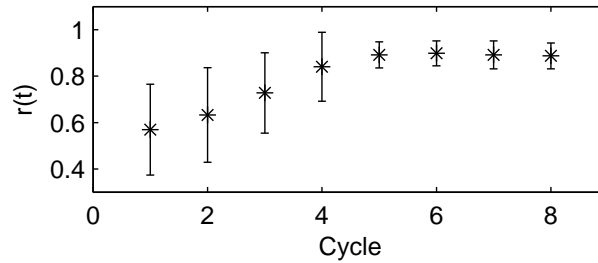


Figure 3.1: *Per* mRNA population as a function of basal transcription rate ν_{sP_0} in uncoupled cells. The solid line represents a simulation where $\nu_{sP_0} = 1$, the dashed line $\nu_{sP_0} = 1.5$, and the dotted line $\nu_{sP_0} = 2$. For ν_{sP_0} below 1.2, *Per* mRNA concentrations exhibit damped oscillations for the ten day period simulated.



(a) *Per* mRNA in the Coupled 5×5 Grid



(b) Order Parameter Radius for the 5×5 Coupled Grid

Figure 3.2: (a) The time series of *Per* mRNA concentration is shown for a single SSA simulation of a 5×5 grid of cells. (b) For 9 SSA simulations of the grid, we show the mean degree of phase coherence with error bars indicating 25% of the standard deviation. The solid line represents simulations where $\nu_{sP0} = 1$, the dashed line $\nu_{sP0} = 1.5$, and the dotted line $\nu_{sP0} = 2$.

Chapter 4

Unraveling the Source of Period-to-Period Variability in Cell Behavior

Cells in the suprachiasmatic nucleus (SCN) display remarkable precision, while either physically or chemically decoupling these cells from each other leads to a dramatic increase in period-to-period variability. Where previous studies have classified cells as either arrhythmic or circadian, our wavelet analysis reveals that individual cells, when removed from network interactions, intermittently express circadian and/or longer infradian periods.

We reproduce the characteristic period distribution of uncoupled SCN cells with a stochastic model of the uncoupled SCN cell near a bifurcation in *Bmal1* transcription repression. This suggests that the uncoupled cells may be switching between two oscillatory mechanisms: the indirect negative feedback of protein complex PER-CRY on the expression of *Per* and *Cry* genes, and the negative feedback of CLOCK-BMAL1 on the expression of *Bmal1* gene. The model is particularly sensitive near this bifurcation point, with only a small change in *Bmal1* transcription repression needed to switch from the stable precision of coupled SCN cells to the unstable oscillations of decoupled individual cells, making this rate constant an ideal target for cell signaling in the SCN.

The work described in this Chapter was published in Kirsten Meeker, Richard Harang, Alexis B. Webb, David K. Welsh, Francis J. Doyle, Guillaume Bonnet, Erik D. Herzog, and Linda R. Petzold. Wavelet measurement suggests cause of period instability in mammalian circadian neurons. *Journal of Biological Rhythms*, 26(4):353–362, 2011. The experimental results were produced in the labs of Prof. Erik Herzog, Washington University, St. Louis and Prof. David Welsh, University of California, San Diego. Our contribution was the stochastic simulation results and their interpretation.

4.1 Experimental Procedure for Collecting Circadian SCN Data

Single cell data were previously published in Liu et al. 2007[68], Ko et al. 2010[62], and Webb et al. 2009[114], and were obtained according to methods described therein. Briefly, SCN neurons with or without various clock gene knock-outs were dispersed from 1-7 day old PER2::LUC reporter mice [124] and cultured for up to 5 weeks at a density of 100-300 cells/sq mm in medium containing 5-10% fetal bovine serum. For comparison to dispersed cultures, neurons were also cultured with relatively intact tissue organization as SCN slices. For imaging, cells were transferred to serum-free, HEPES-buffered medium containing B27 supplement and luciferin, placed on the stage of an inverted microscope kept at 36-37 °C, and imaged with a low-noise CCD camera. Circadian clock function was measured as a time series of PER2::LUC bioluminescence intensities for single cells in 30-60 minute intervals over 6-8 days. For additional details on bioluminescence imaging methods, see Welsh et al. [117, 118]. All animal procedures were approved and performed in accordance with local institutional guidelines as indicated in Webb et al. 2009 [114], Liu et al. 2007 [68], and Ko et al. 2010 [62].

These data were collected in two different labs. Although methods used to collect these data were broadly similar, a number of differences could have affected

the results. For example, Webb et al. used mice of a pure C57/BL6 genetic background instead of a mixed background, lower cell density of 100 cells/sq mm instead of 300 cells/sq mm, and started imaging sooner at 4 days in culture instead of 2-7 weeks in culture. Accordingly, the wild type datasets from the two different labs were analyzed separately [68, 114].

4.2 Wavelet Analysis Reveals Non-Stationary Periods in PER2:LUC SCN Cells

We use CWT analysis as described in Chapter 2 to recover period information from the bioluminescence recordings of PER2:LUC SCN cells. Figure 2.2 displays examples of the initial CWT analysis performed on three individual cells; the traces in the upper panels correspond to the heatmaps in yellow, white, and red in the lower panels, which are used to generate the ridges highlighted in green. Each ridge point indicates the dominant oscillatory period for the cell at the indicated time; this analysis is repeated across all cells in the data set (see Supplement of [73] for more examples).

For oscillators that exhibit strongly stochastic behavior, distributional information about the period of the oscillator is much more relevant than examining the time-frequency evolution of a single realization – as proposed in [84] and used

in [13]. We utilize both period variability histograms and period distribution plots to examine this distributional behavior of SCN oscillators. Period variability histograms (Figure 4.3) display the period variability of various populations of SCN cells as inferred by CWT analysis; each cell's instantaneous period over time was estimated individually using the CWT as described above, and the standard deviation of that period over time was calculated to estimate the stability of the cell's oscillations. The results using CWT analysis are consistent with those described in [53] and [11]: dispersed SCN cells display a significantly broader range of period standard deviations than coupled SCN cells. Note that the slice data from both labs (Figure 4.3, A and C) displays a significantly tighter cluster of variances than the corresponding dispersed data, but that the modal variance is not zero, indicating that there is some inherent variability in the periods even of coupled SCN cells. Analysis of cells decoupled by physical dispersion (Figure 4.3, B and D) illustrate that the range of period variability increases significantly in the absence of intracellular communication.

The distribution of instantaneous periods across time for a pooled population of SCN oscillators is displayed in period distribution plots. A simple histogram of instantaneous periods is created for each cell, and a population histogram is assembled to visualize the period distribution over a population of cells. Figure 4.4 (A and B) compares the period distribution of coupled and dispersed cells. As

expected from previously published results, the dispersed cell period distribution is wider than that of coupled cells in an SCN slice. Dispersed cells spend half of their time at periods between 23-42 hrs. (data from [114]) or 22-30 hrs. (data from [68]), while coupled cells spend half of their time at a narrower range of periods between 24-29 hrs. The period distribution of dispersed cells also has a long period tail up to 48-53 hours, while at the same time there are few periods shorter than 18 hours. The long period tail observed here by using wavelet analysis is a distinguishing characteristic of the underlying stochastic processes driving the oscillations.

While cellular heterogeneity is one possible explanation for the overall population distribution of periods, both direct examination of individual cell plots (see Figures 2.2, 4.1, and 4.2) as well as analysis of the frequency distribution of individual cells reveal that an assumption of heterogeneity does not appear to be required to explain these data. Most dispersed wild-type SCN cells have circadian periods (20-30 hrs.) most of the time. Across all cells, 79.4% of all recorded oscillations are in the circadian range. However, the majority of cells (67.6%, 255 out of 377) also exhibit non-circadian behavior: a dominant period outside of 20-30 hrs. There are only a few cells (5.8%, 22 out of 377) that have no dominant period within the circadian range. We therefore conclude that a heterogeneous population of cells oscillating with different periods is not needed to reproduce the

distribution of periods observed in biological cells (Figure 4.4). Meeker et al. [73] and its supplementary material provide a thorough statistical analysis supporting this claim.

4.3 Modeling Provides a Possible Mechanism

An increase in period variability can be achieved either by reducing the number of molecules in the stochastic model, or by adjusting model parameters to be near a bifurcation point where oscillations are less stable. In this study we consider both techniques and show results from the following variants of a discrete stochastic version of the Leloup and Goldbeter model [66]: (1) as the number of molecules is reduced (2) near a non-oscillatory bifurcation point of the mean *Period* gene (*Per*) transcription rate ν_{sP} (3) near an unstable range in the *Bmal1* gene transcription repression K_{IB} , (4) and near an unstable range in the mean *Bmal1* gene transcription rate ν_{mB} .

Surprisingly, by lowering the molecular count alone, we are not able to reproduce the biological period distribution. As the molecular population is lowered the period distribution does widen (Figure 4.4-C), but does not exhibit the long-periods observed in the biological data. Next we test the model near a non-oscillatory bifurcation point of mean *Per* transcription rate ν_{sP} . This model

variation was used in [104] to produce a heterogeneous population of cells with a desired percentage of oscillatory and non-oscillatory cells. It has the advantage that increasing *Per* transcription through inter-cellular coupling restores rhythmicity to all the cells, which is a necessary condition for inter-cellular synchrony. Approaching the ν_{SP} bifurcation widens the period distribution (Figure 4.4-D); however the long periods which we have shown to be significant in our analysis in the previous section are not reproduced.

To determine how the stochastic model can be made to produce the long periods, bifurcation analysis of the deterministic Leloup and Goldbeter model is employed. Our analysis identifies two sets of parameters that are capable of producing the longer periods observed in the dispersed cell data. The first set (Figure 4.5 left column) is associated with the PER-CRY feedback loop and requires an order of magnitude change in value to produce the period range. The second set (Figure 4.5 right column) is associated with the CLOCK-BMAL1 feedback loop or global scale factors, and produces the observed period range with less than an order of magnitude change. Global parameters ν_{sTot} and k_{sTot} change the transcription and protein production rates of all three key genes. Changes in these global parameters are reflected in the *Bmal1* mRNA transcription rate and BMAL1 protein production rate, and so produce the same 2 branch bifurcation behavior found in parameters affecting the production of *Bmal1* mRNA.

For the second set of parameters, the period versus parameter functions all have two oscillatory branches connected by an unstable oscillatory segment. Leloup and Goldbeter [67] identified each of the two oscillatory branches with one of the feedback loops present in the circadian clock. [97] demonstrated that a simple model consisting of interlocked positive and negative feedback loops could behave as either a bistable switch or an oscillator depending on the relative strengths of the two feedback loops. Selecting parameter values that allow switching between the oscillatory branches provides a mechanism by which longer periods may be generated by the model.

The *Bmal1* transcription repression K_{IB} and transcription rate ν_{mB} are chosen from the second group of parameters for their maximum period value and sensitivity. Stochastic simulation results (Figure 4.4-E) show that as K_{IB} is increased the period distribution of the stochastic model widens, creating a longer tail on the distribution of infradian periods, and at the same time increasing the mean period.

To quantify the difference between period distributions, the Kullback-Leibler (KL) divergence [65] is used. The Kullback-Leibler divergence provides a measure of “distance” or “divergence” between statistical densities in terms of relative information gain. Smaller values of the KL divergence indicate two distributions that are more nearly similar. Increasing the *Bmal1* transcription repression K_{IB}

produces the lowest KL divergence (Table 4.1) while preserving oscillatory behavior and hence produced the best period distribution fit among the models studied (Figure 4.4).

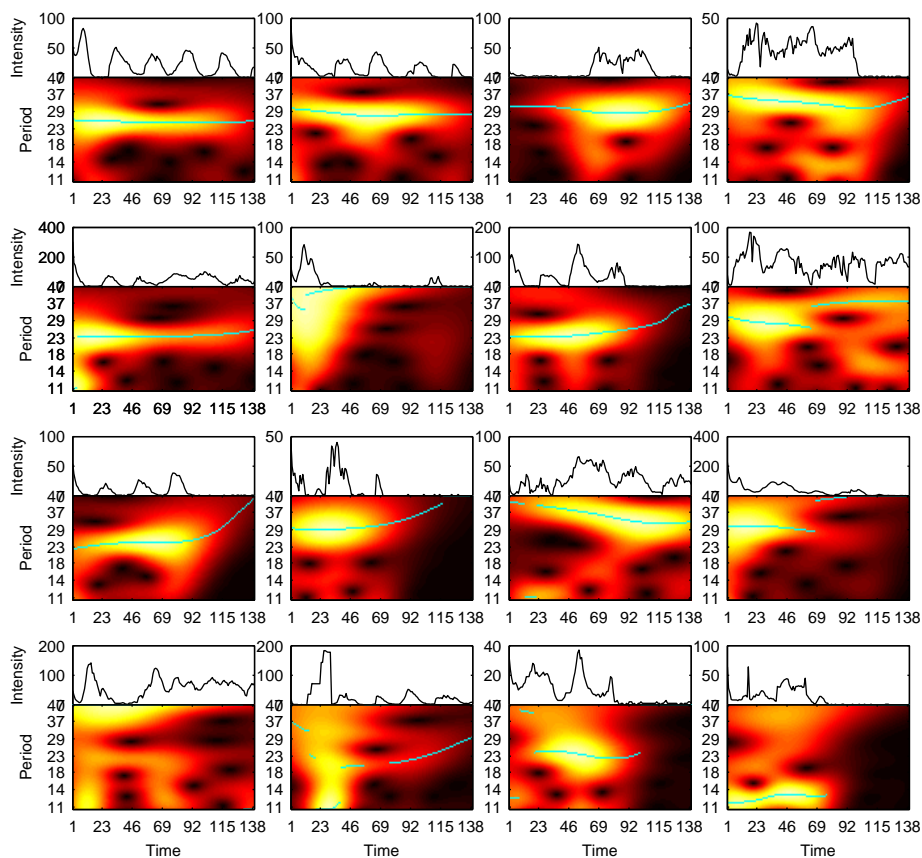


Figure 4.1: Magnitude heat maps resulting from Wavelet transform show the range of circadian behaviors possible in dispersed SCN cells sampled from $n=322$ cells from Webb et al. 2009 [114].

Table 4.1: Kullback-Leibler divergence compares period distributions of stochastic model variants with those observed in both Webb et al. [114] and Liu et al. [68] for dispersed wild-type cells. Smaller values of the KL divergence indicate two distributions that are more similar.

Model number of molecules, Ω	12	25	50	100	200
Webb et al. (2009)	1.56	10.8	12.3	12.2	17.2
Liu et al. (2007)	1.29	4.44	5.47	6.08	8.35
Model <i>Per</i> transcription, ν_{sP}	1.1	1.2	1.3	1.4	1.5
Webb et al. (2009)	0.38	1.66	2.88	4.93	10.8
Liu et al. (2007)	0.73	1.32	2.02	2.76	4.44
Model <i>Bmal1</i> repression, k_{IB}	2.2	3.5	4.0	5.5	6.5
Webb et al. (2009)	10.8	5.21	1.34	1.62	4.74
Liu et al. (2007)	4.44	2.97	1.48	2.89	6.19
Model <i>Bmal1</i> degradation, ν_{mB}	0.65	0.7	0.75	0.8	
Webb et al. (2009)	1.88	10.9	10.0	10.8	
Liu et al. (2007)	1.86	4.68	3.83	4.44	

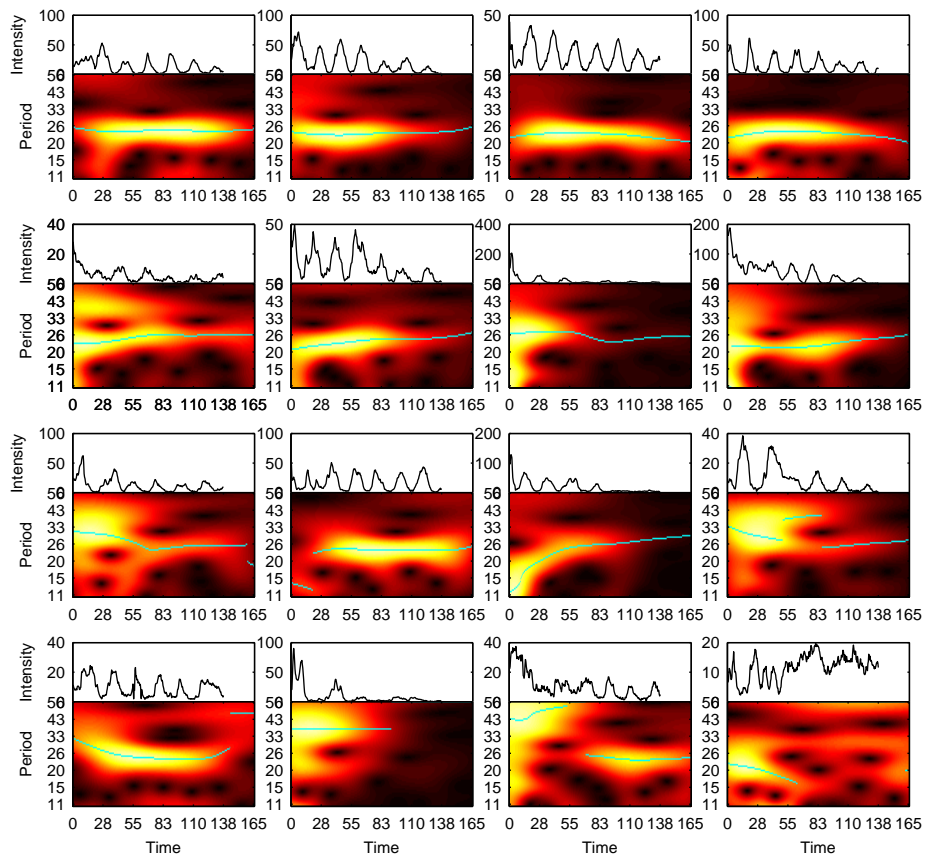


Figure 4.2: Magnitude heat maps resulting from Wavelet transform show the range of circadian behaviors possible in dispersed SCN cells sampled from $n=310$ dispersed cells from Liu et al. 2007 [68].

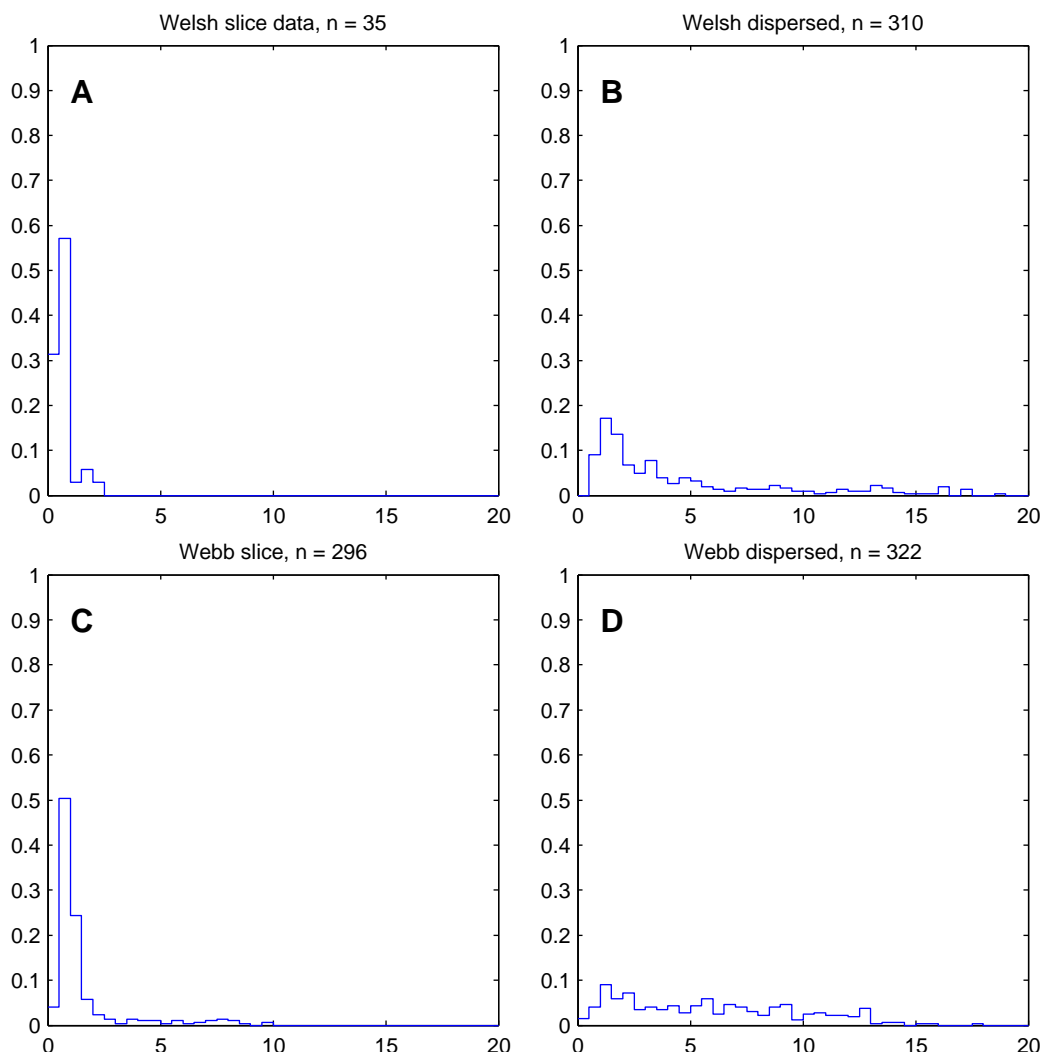


Figure 4.3: Histograms showing the period variability (standard deviation) of coupled and dispersed cells from Webb et al. [114] (C-D) and Liu et al. [68] (A-B). Coupled cells (slice; A,C) have less period variability than dispersed cells (B,D).

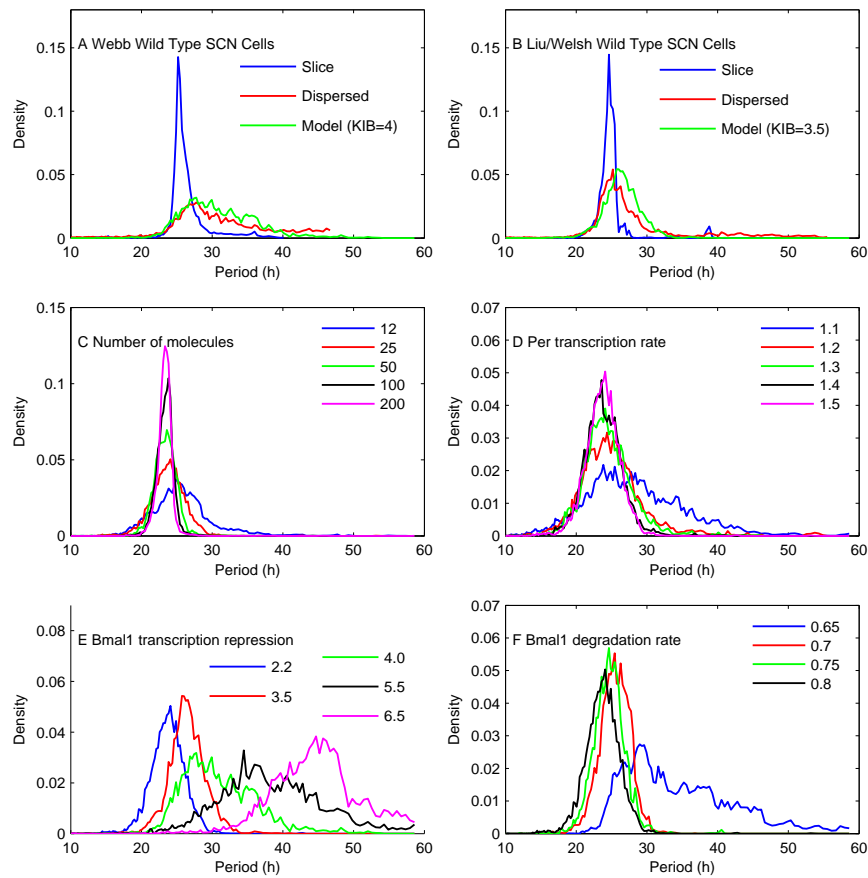


Figure 4.4: Period distributions of dispersed and coupled SCN cells and stochastic model with parameter variations.

Figure 4.4: (A-B) The period distributions of dispersed cells from both labs are wider than that of coupled cells (SCN slice) and have a long period tail of up to 48-53 hours. The $K_{IB} = 3.5$ & 4.0 model distributions show the presence of long periods consistent with the biological data. (C) Decreasing the number of molecules in the stochastic model fails to produce the long period tail observed in the biological data. (D) Decreasing the *Per* transcription rate to very close to the bifurcation point ($\nu_{sP} = 1.1$) begins to produce a long period tail, but the period is less likely to be in the circadian range (24-19 hrs.) than the biological data. (E) Increasing the Bmal1 transcription repression switches the period from the circadian range to long periods (40-50 hrs. for $K_{IB} = 6.5$). (F) Decreasing the Bmal1 degradation rate also produces a switch, but with less probable long periods.

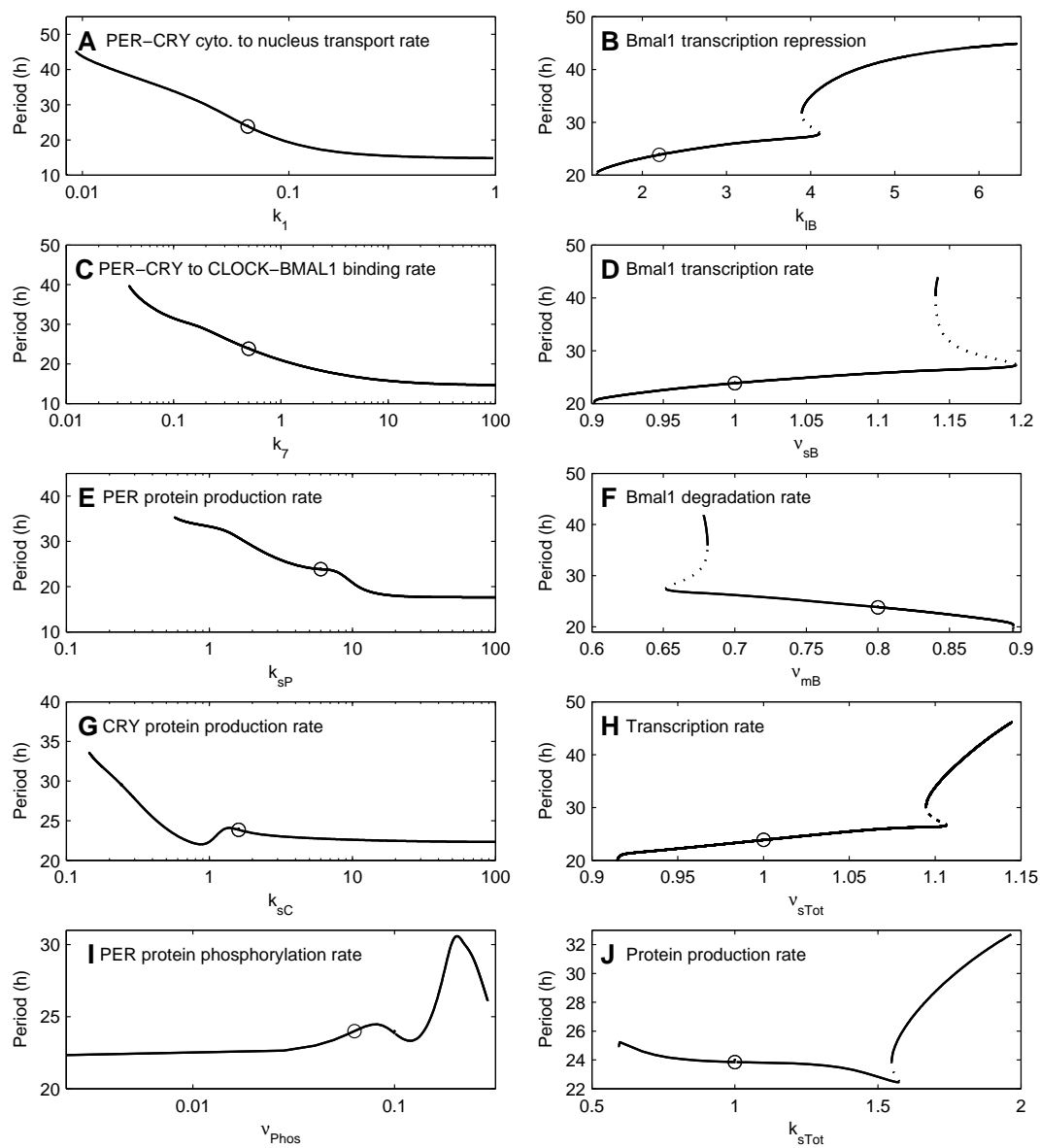


Figure 4.5: PER-CRY and CLOCK-BMAL1 feedback loop parameters and global scale factors that produce long periods

Figure 4.5: PER-CRY feedback loop parameters (left) and CLOCK-BMAL1 feedback loop parameters and global scale factors (right) that produce long periods. The plots on the left have one stable oscillatory branch and require an order of magnitude change to produce long periods. In contrast, the plots on the right have two stable oscillatory branches (solid line) connected by an unstable oscillatory range (dashed line) and require less than an order of magnitude change to produce long periods.

Chapter 5

Phase Tumbling - A Theory of Entrainment

Shift work or transmeridian travel can desynchronize the body's circadian rhythms from local light-dark cycles. The mammalian suprachiasmatic nucleus (SCN) generates and entrains daily rhythms in physiology and behavior. It is comprised of approximately 20,000 neurons that synchronize to each other, and entrain to ambient light cycles [52][111]. Vasoactive intestinal polypeptide (VIP), a neuropeptide released in the SCN as a function of circadian time and light intensity [95][96][91], plays a critical role in this circadian synchronization.

In the absence of VIP or its receptor, VPAC2R, SCN neurons fail to synchronize to each other and consequently many daily rhythms of the organism are

lost [50][25][12][22][71]. The addition of VIP to SCN cultures induces the production of *Period (Per) 1* and *2* [79], two genes implicated in light-induced resetting [5][102][103], and shifts rhythms in behavior and SCN physiology [82][112][86][75][9]. Notably, daily addition of VIP or an agonist to the VIP receptor, VPAC2R, entrains rhythms in SCN explants and *Vip*^{-/-} SCN neurons [9][12]. Thus, VIP is thought to play a role in both the synchronization of SCN cells when the organism is in the dark, and the entrainment of the SCN when the organism is exposed to a light cycle.

Paradoxically, we found that VIP, implicated in synchrony among SCN cells, can also desynchronize them. The degree and duration of desynchronization among SCN neurons depended on both the phase and the dose of VIP. A model of the SCN consisting of coupled stochastic cells predicted both the phase- and the dose-dependent response to VIP, and that the transient phase desynchronization, or “phase tumbling”, could arise from intrinsic, stochastic noise in small populations of key molecules.

Exposure to a brief light pulse has been shown to reduce the amplitude of circadian rhythms in humans [59], insects [119][34] and cell lines expressing transgenic melanopsin [85][105]. Lower amplitude oscillations have been associated with larger shifts in behavioral and physiological rhythms [51][110] and the ability to entrain to a wider range of periods [3][24]. Our model predicted that

desynchronization in response to VIP would accelerate entrainment to a shift in environmental cycles. We tested this experimentally using a pretreatment of VIP during the day before a shift in either a light cycle *in vivo* or a temperature cycle *in vitro*. The VIP pretreatment approximately halved the time required for mice to reentrain to an 8-h shifted light schedule and for SCN cultures to reentrain to a 10-h shifted temperature cycle. This has the potential to reduce jet lag.

The work described in this Chapter was published in Sungwon An, Rich Harang, Kirsten Meeker, Daniel Granados-Fuentes, Connie A. Tsai, Cristina Mazuski, Jihee Kim, Francis J. Doyle, Linda R. Petzold, and Erik D. Herzog. A neuropeptide speeds circadian entrainment by reducing intercellular synchrony. *Proceedings of the National Academy of Sciences*, 2013. The experimental results were produced in the lab of Prof. Erik Herzog, Washington University, St. Louis. Our contribution was the stochastic simulation results and a “phase tumbling” theory of how the SCN entrains to a light cycle.

5.1 Experimental Results

5.1.1 VIP reduces the amplitude of circadian rhythms in the SCN by reducing synchrony

As part of an analysis of VIP-induced phase shifts of the SCN [85], we noted that the peak-to-trough amplitude of SCN rhythms reliably decreased and then gradually recovered after application of VIP (Fig. 5.1a). Replacing the medium with three full exchanges 1 h after VIP application yielded similar results, indicating that the effects persisted many days after the added VIP was gone (Fig. 5.2a). We found that VIP reduced the peak-to-trough amplitude of PER2 rhythms with a half-maximal response near 150 nM and saturation above 10 μ M (Fig. 5.1b). Within this range, a 10-fold increase in VIP concentration halved the PER2 amplitude ($r^2 = 0.99$, $n = 31$ explants). VIP reduced the amplitude similarly when it was applied on the rising or falling phases of the PER2 cycle, but more when PER2 levels were at their lowest around circadian time (CT) 22 (Fig. 5.1c). Consistent with prior reports [30][38], PER2 amplitude was unaffected by vehicle, 30 μ M glutamate, a major mediator of photic input to the SCN (Fig. 5.2b), or 1 μ M gastrin releasing peptide (GRP), another neuropeptide expressed and released in the SCN (Fig. 5.1d). Thus, at concentrations above 100 nM, VIP

sufficed to reduce the amplitude of circadian rhythms in the SCN in a phase- and dose-dependent manner.

5.1.2 VIP reduces the synchrony of SCN populations

The amplitude reduction recorded from the population of SCN cells could reflect phase dispersion between rhythmic SCN cells, reduced rhythmicity of individual cells, or both. To distinguish between these possibilities, we measured the effect of VIP on rhythms in individual neurons in SCN slices. Whereas vehicle had no measurable effect on rhythmicity or synchrony, 150 nM or 10 μ M VIP reduced the synchrony among SCN neurons (Fig. 5.3; Raleigh test r values before and after vehicle: 0.93 ± 0.01 and 0.91 ± 0.07 , $n = 2$ cultures; before and after 150 nM VIP: 0.84 ± 0.03 and 0.51 ± 0.07 , $n = 5$; before and after 10 μ M VIP: 0.77 ± 0.03 and 0.25 ± 0.12 , $n = 2$) and modestly reduced the peak-to-trough amplitude of individual cells (measured two cycles after treatment; vehicle: 0.94 ± 0.04 , 150 nM VIP: 0.73 ± 0.03 , $P > 0.05$, Student's t test; Wilcoxon-Mann-Whitney rank sum test for differences in phase clustering; vehicle, $P > 0.07$ in two cultures ; 150 nM VIP, $P > 1 \times 10^{-3}$ in five cultures; 10 μ M VIP, $P > 0.01$ in two cultures). The amplitude reduction of individual cells following 150 nM VIP accounts for less than half of the amplitude reduction seen at the population level.

Therefore, VIP-induced desynchrony among SCN cells is required to explain the reduced amplitude of ensemble PER2 rhythms.

5.1.3 Constant light requires VIP to reduce circadian amplitude *in vivo*

These *in vitro* results led us to test whether VIP plays a role in modulating circadian amplitude *in vivo*. Because prolonged constant light (LL) has been reported to desynchronize rhythms among SCN cells and produce arrhythmic locomotor behavior [80], we recorded wheel running from wild-type (C57BL/6, n = 18) and Vip-deficient ($Vip^{-/-}$, n = 15) mice maintained in LL for 40 days followed by 10-11 days in constant darkness (DD). Control mice showed a marked reduction of their daily peak-to-trough amplitude in LL compared to DD (LL/DD ratio: 0.2 ± 0.04), while amplitude changed little in $Vip^{-/-}$ mice (LL/DD ratio: 0.94 ± 0.17 , $P > 0.0005$, comparison of fold change in amplitude between wild type and $Vip^{-/-}$, Student's two tailed t-test; Fig. 5.4). Therefore, VIP plays a critical role in reducing the amplitude of locomotor activity rhythms in response to light.

5.2 Theory and Simulation

How can VIP both synchronize and desynchronize circadian cells? Underlying this apparent contradiction may be a phase tumbling mechanism similar to the ‘run and tumble’ mechanism of bacterial chemotaxis [21] where SCN neurons receiving VIP stimulation at a phase far from the phase angle of entrainment would ‘tumble’ their phases. This would result in reduced synchrony among the circadian cells. In contrast, SCN neurons receiving VIP stimulation near their phase angle of entrainment would ‘run’ towards it.

5.2.1 A computational model of circadian desynchronization predicts faster entrainment

A fundamental consequence of the phase tumbling hypothesis is that a desynchronized SCN should entrain faster than a synchronized SCN to a large shift in the environmental cycle. To test this, we generated a cell model which is a stochastic adaptation of Leloup and Goldbeter’s deterministic model of circadian gene regulation [66] that includes coupling [104] and a mechanism for light input [14]. In our simulations, cells were initialized with either random or synchronized phases. The light cycle was simulated with daily release of VIP. The phases of the cells were tracked by the time of their daily PER protein peak using the Morlet

continuous wavelet transform [61]. Our stochastic model of the SCN predicted that cells with random initial phases would entrain, on average, 1-5 days faster (depending on the size of the scheduled shift) than cells with synchronized phases. Further, it predicted that VIP exposure would reduce the amplitude of the synchronized population by reducing synchrony (Fig. 5.5). Thus, importantly, the stochastic model can explain both the desynchronization and rapid entrainment of the SCN by VIP.

The phase tumbling hypothesis was motivated by the phase response distribution (PRD) (Fig. 5.6) of our stochastic model. A PRD is similar to a phase response curve (PRC), in that it plots the change of phase as the result of a pulse of light (represented in our model as a pulse of VIP) at a given time. It differs from the PRC in that it shows the distribution of the responses, as opposed to the aggregate response. There are a number of important features of this PRD. First, note that the region that is roughly between CT 2 and CT 10 is stable, in the sense that a pulse of light is unlikely to shift the phase outside this region and is in fact likely to shift the phase towards the phase angle of entrainment near CT 4. Second, there is greater phase dispersion outside this region, with greatest phase dispersion occurring near CT 22. In short, given a pulse of light between CT 2 and CT 10, the circadian cells are ‘running’ towards CT 4 (but occasionally

tumbling along the way). In contrast, given a pulse of light elsewhere, the cells are more likely to be ‘tumbling’ their phases.

To see the effects of desynchronization using the PRD, consider starting with a synchronized system and applying a pulse of light at CT 19.5 and every 24 hours thereafter. The full distribution information available in the PRD is used to determine the probability that a cell at a given CT will shift to any other CT. To do this, we bin the CTs and form a histogram, as shown in Fig. 5.7, then we apply the entrainment signal. The left column of the figure shows the phase distribution at 24 hour intervals for cells that are completely desynchronized when they receive the initial entrainment signal. The right column illustrates the process of entrainment to a large shift in the environmental cycle for cells that are initially synchronized: it is clear that the cells first desynchronize and then entrain, hence the total time to entrainment is longer than if they had started out desynchronized.

Intrinsic stochasticity, due to small populations of key chemical species, naturally results in a PRD that is consistent with phase tumbling. The structure of the Leloup and Goldbeter [66] model suggests the source of the variability in the phase dispersion. The rate of change of *Per* mRNA in the nucleus is defined as the sum of three terms that characterize: 1) the transcription rate, 2) the transport rate from the nucleus to the cytoplasm, and 3) the *Per* mRNA degradation

rate. Augmenting VIP increases the variability of nuclear *Per* mRNA accumulation when nuclear-cytoplasmic transport rates and degradation rates are low (near CT22), while the effect of VIP application near CT4, when transport and degradation rates are high, is much smaller.

5.3 Experimental Validation of Phase Tumbling Hypothesis

5.3.1 VIP speeds photic entrainment in vivo

Our simulation results predicted that VIP-induced reduction of synchrony could accelerate entrainment to changes in the light schedule. To test this possibility, we implanted cannulae aimed at the SCN of adult mice. Because VIP has been shown to shift locomotor rhythms in vivo depending on the time of application, we chose to deliver VIP at CT3 when it does not shift circadian rhythms [82]. This avoids the potential confounds of VIP inducing shifts that could speed or slow adjustment to a new schedule. We maintained wild-type mice in 12 h: 12 h light: dark cycles (lights on from 7:00 a.m. to 7:00 p.m.), for 7 days before and 7 days after cannulation of the SCN. After a week, mice received either 20 (n = 4) or 200 pmole (n = 10) VIP or vehicle (artificial cerebral spinal fluid; n

= 12) at 10:00 a.m. Lights were turned off after the injection and then turned on from 11:00 p.m. to 11:00 a.m., corresponding to an 8 h-advance in the light cycle. By using dim lights (1.0×10^{15} photons/s/cm²), we reduced the confound of light suppression (masking) of locomotor activity. This had the added advantage of slowing entrainment to a shifted light schedule so that we could accurately measure the rate of entrainment. The animals injected with VIP rapidly shifted their onset of activity and required fewer days to entrain than the vehicle-injected animals (mean of VIP-injected animals: 4.5 ± 0.4 days, $n = 14$; vehicle-injected animals: 7.8 ± 1 days, $n = 12$, $P > 0.005$, Student's two tailed t-test; Fig. 5.5a-c). These results show that VIP sped entrainment to a large advance in the light schedule.

5.3.2 VIP speeds temperature entrainment of the SCN *in vitro*

To determine whether VIP directly accelerates entrainment of the SCN, we measured the days required for SCN cultures to synchronize their circadian rhythm to a 10-h advanced temperature cycle. We tracked the time of peak PER2 expression in SCN explants maintained in a 12h:12h warm: cool cycle (36.5 °C starting at 6 a.m, 35 °C starting at 6:00 p.m.) for 8 days followed by a 10-h advanced warm: cool cycle (8:00 p.m. warm, 8:00 a.m. cool) for 9 days and then 4 days

at 36.5 °C. SCN were treated with either 10 μ M VIP or vehicle at 4:00 p.m., 11 h prior to the shift in the temperature cycle. We chose to deliver VIP at the same relative time as the *in vivo* experiment (ZT 3), a time when it also produces minimal shifts *in vitro* (18-21). SCN were defined as entrained to the new cycle once the phase relationship between the daily warming and peak PER2 was stable for at least $48\text{h} \pm 0.25\text{ h}$ with a phase of 17.2 ± 1 (VIP-treated cultures) or 15.5 ± 1 (vehicle-treated cultures). VIP-treated SCN cultures entrained within 4.2 ± 0.4 days to a mean phase of 17.2 ± 0.5 (Rayleigh test, $P > 0.005$, $r = 0.8$, $n = 5$), whereas controls took longer (9.6 ± 2.1 days, $P < 0.05$, Student's two tailed t-test; Fig. 5.5d-f) and had more broadly distributed peak phases (mean phase: 12.6 ± 1.7 , $P > 0.05$, $r = 0.3$, $n = 5$). Indeed, two of the vehicle-treated cultures (40%) did not appear to be fully entrained even 13 days after the start of the shifted schedule. Thus, VIP pretreatment similarly doubled the speed of the entrainment to a new environmental cycle of behavior and of the SCN.

We have discovered that treatment with VIP can reduce synchrony among SCN cells *in vitro* in a phase- and dose-dependent manner. Our experimental and modeling data suggest that the phase-dependent desynchrony following treatment with VIP results from the variable shifts experienced by individual cells in a process that we call phase tumbling. Phase tumbling is a direct consequence of stochastic variation in small numbers of key molecules within the circadian

clock. The phase tumbling model explains faster entrainment without explicitly weakening cell-cell communication or coupling. A recent model of the circadian clock in plants also noted that introduction of stochastic molecular noise yielded less synchrony among oscillators and faster entrainment [46].

These results highlight VIP release within the SCN as a target for potential therapies aimed at improving circadian synchronization during travel or shift work, and we posit that appropriate administration of light could mimic these results. VIP reduces the amplitude of SCN rhythms more at CT22 than at other times, and when applied daily entrains the SCN to a time of relative phase stability at CT4. This suggests a strategy for reducing jetlag: arrange to arrive at the destination at a time when you will receive light exposure near CT22. At that circadian time, the dependence of the mammalian circadian clock's period on nuclear-cytoplasmic shuttling of clock proteins and mRNA degradation [61][29][57][120] provides a sensitive point for cell-cell variation.

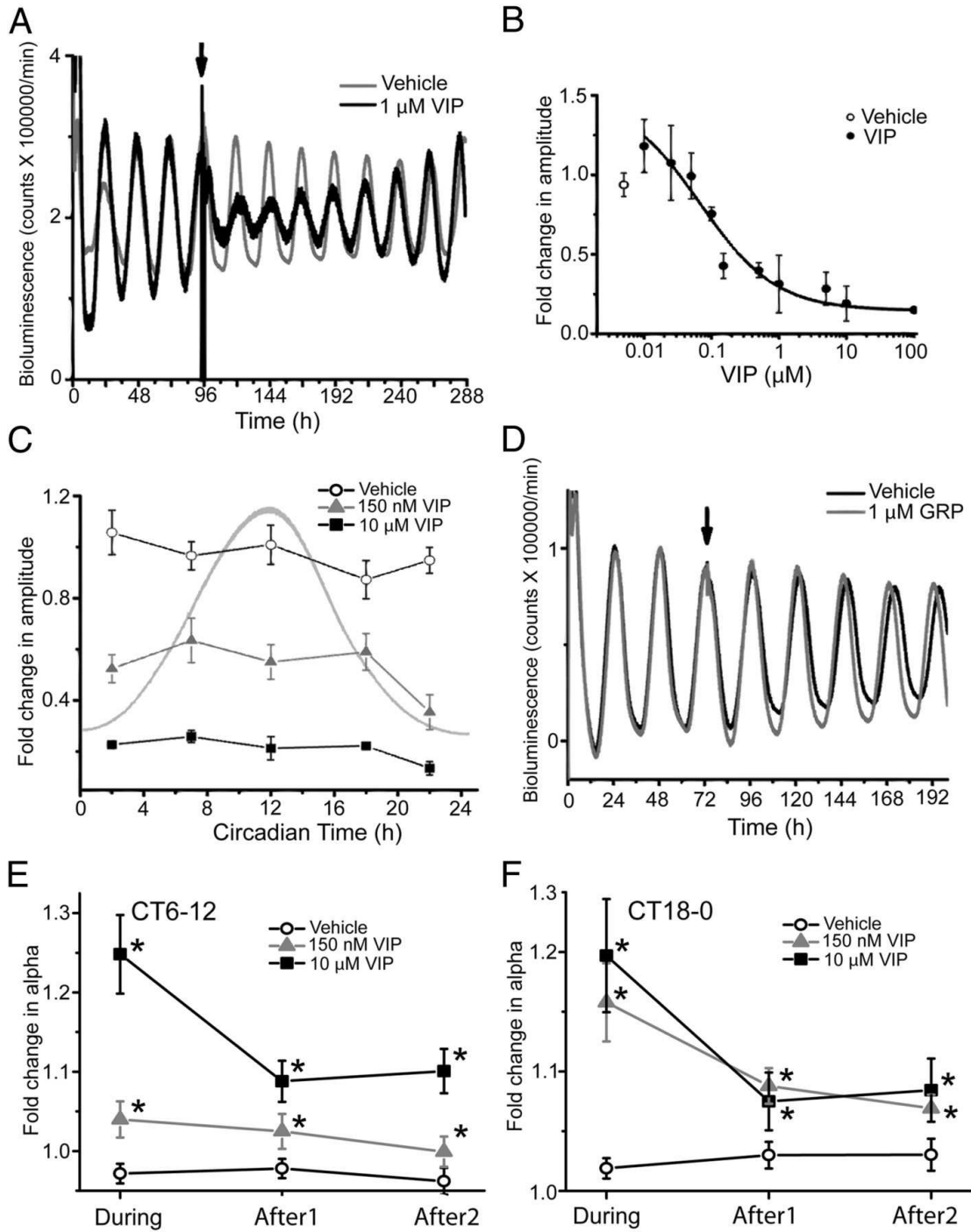


Figure 5.1: VIP dose-dependently reduces the amplitude of circadian rhythms in the SCN.

Figure 5.1: (A) Representative detrended bioluminescence traces from PER2::LUC SCN explants were treated with 1 μM VIP (solid line) or vehicle (shaded line) delivered near the peak of PER2 expression (CT12, arrow). Note that the amplitude of the VIP-treated SCN decreased and, then, gradually recovered. Each trace was normalized to the peak before treatment. (B) The dose-dependent amplitude decrease (mean \pm SEM; $n = 35$ cultures at each dose) by VIP application at CT12. Between 150 nM and 10 μM VIP, the amplitude decreased linearly with logarithmic increases in VIP concentration. Data were fitted with a logistic function (solid line). Amplitude was measured as the trough-to-peak magnitude 48 h after VIP application. (C) The amplitude reduction of PER2 cycling (mean \pm SEM) was greater following 10 μM VIP (squares; $n = 20$) than 150 nM VIP (triangles; $n = 16$) at all times ($P < 0.00001$, $F_{6,66} = 38.53$, $n = 74$; two-way ANOVA with a Scheffé post hoc). Notably, 10 μM VIP delivery at CT22 had a larger effect on amplitude than at other times ($P < 0.03$, $F_{4,14} = 3.87$, $n = 19$; one-way ANOVA with a Scheffé post hoc). Vehicle (open circles) did not reduce the amplitude at any time. The shaded line corresponds to a PER2-expression rhythm peaking at CT12.

Figure 5.1: (D) Representative bioluminescence traces from SCN explants treated at the peak of PER2 expression (arrow) showing that another neuropeptide, 1 μ M gastrin-releasing peptide (GRP) (solid line), did not reduce amplitude compared with vehicle (shaded line) applied at CT12. (E) VIP application transiently broadens the waveform of PER2 expression. The fold change (mean \pm SEM) in the duration (α) of PER2 expression is plotted relative to the PER2 duration on the day before treatment. When applied near the peak of PER2 (E), VIP dose-dependently increased the width of PER2 expression on the day of treatment and for the 2 d after (10 μ M VIP, squares, n = 3; 150 nM VIP, triangles, n = 8; vehicle, circles, n = 8; $P < 0.000003$, $F_{2,18} = 32.5$, two-way ANOVA with a Scheffé post hoc). The peak broadening effect of VIP decreased with days after treatment ($P < 0.05$, $F_{2,18} = 2.8$, Two-way ANOVA with a Scheffé post hoc). Similarly, when applied near the trough of PER2 (F), 10 μ M VIP (n = 12) and 150 nM VIP (n = 7) increased the width of daily PER2 expression compared with vehicle (n = 8; $P < 0.0005$, $F_{2,26} = 8.3$, two-way ANOVA). This effect on α persisted for the 2 d after VIP application ($P = 0.006$, $F_{2,26} = 5.5$, two-way ANOVA).

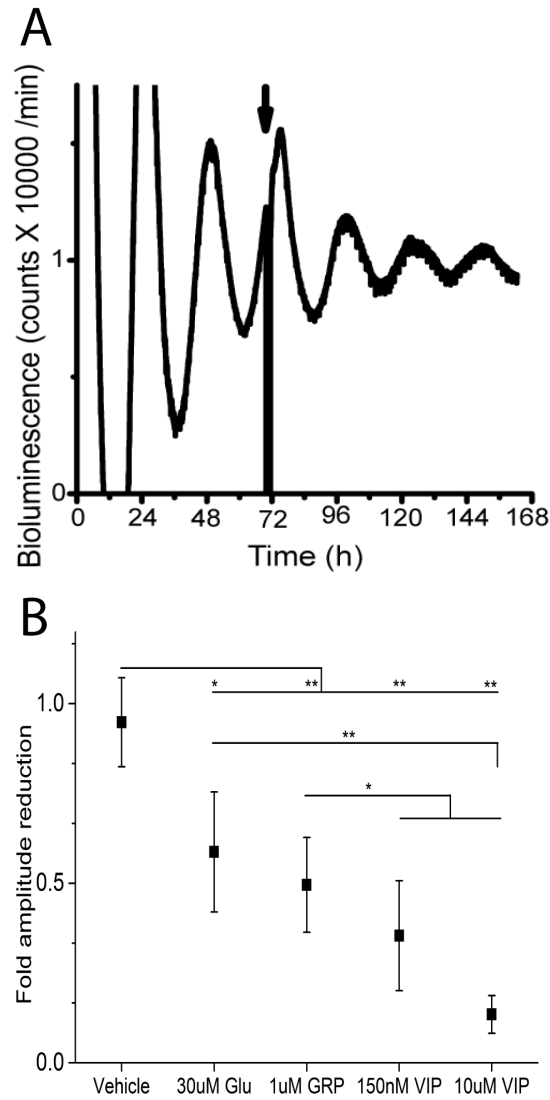


Figure 5.2: VIP reduces the amplitude of PER2 rhythms after three washes

(A) VIP reduces the amplitude of PER2 rhythms after three washes. A representative trace from a SCN explant treated with 10 μ M VIP at CT11 (arrow), followed by three full medium changes after 1 h, shows that the amplitude of PER2 rhythms decreased rapidly and slowly recovered similar to that in cultures treated without removing VIP from the dish.

Figure 5.2: (B) Compared with VIP, stimulation with 30 μ M glutamate (Glu) or 1 μ M gastrin-releasing peptide (GRP) at CT22 modestly reduced the amplitude of PER2 expression on the day after application (*P < 0.05, **P < 0.01; one-way ANOVA followed by a Scheffé test; n = 47 SCN per treatment).

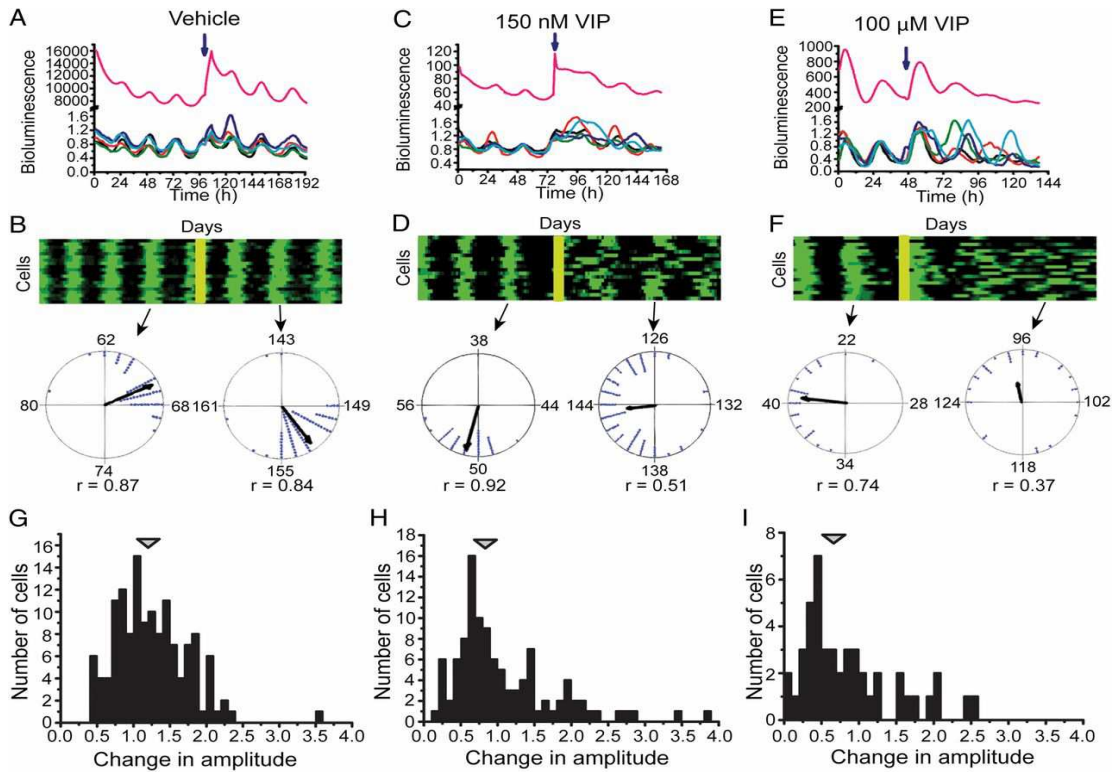


Figure 5.3: VIP dose-dependently reduces circadian synchrony among SCN cells.

(A) PER2::LUC bioluminescence traces of five randomly selected cells treated with vehicle (blue arrow). Note that the cells retained their phase relationships and amplitudes so that their summed expression (purple trace) shows a circadian rhythm with sustained amplitude.

Figure 5.3: (B) A raster plot shows the daily increase (green) and decrease (black) in PER2 expression from 20 representative cells in the same SCN slice treated with vehicle (yellow bar). Two Rayleigh plots show distribution of phases among cells ($n = 140$) in this SCN on the day before and 1 d after vehicle administration. Each dot represents the time of daily peak PER2 expression for one cell. Note that the length of the mean vector (r) did not change following the treatment, indicating that the cells remained synchronized. In contrast, treatment with VIP reduced synchrony among SCN cells depending on the concentration of VIP as illustrated by (C and E) representative PER2::LUC traces from 5 cells and (D and F) raster plots from 20 representative cells and Rayleigh plots before and after VIP administration. Note that, compared with vehicle (G), VIP-treated cells in each of these representative cultures remained rhythmic with modest effects on their peak-to-trough amplitude (H and I), but with reduced synchrony.

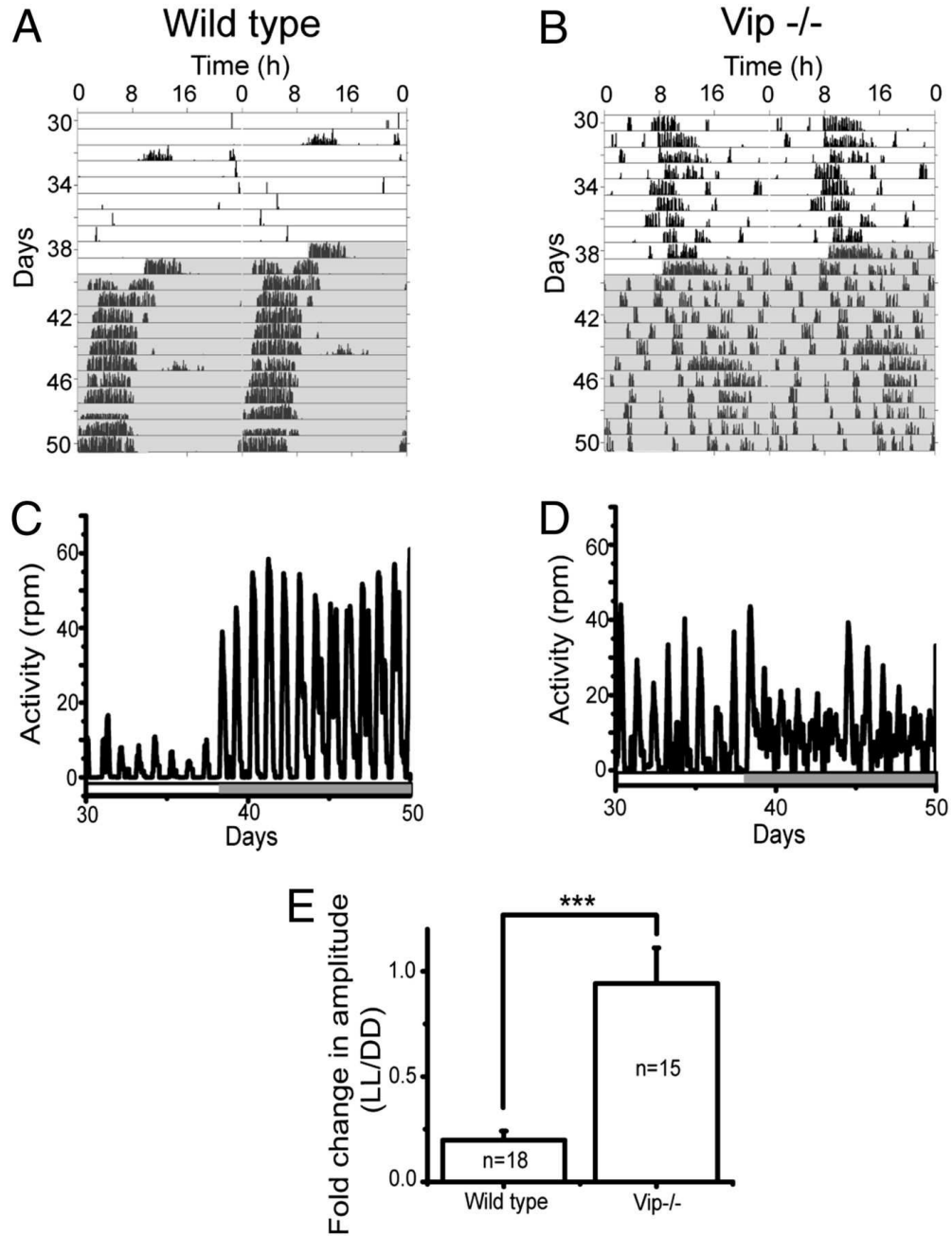


Figure 5.4: VIP mediates the amplitude reduction of locomotor rhythms by constant light (LL).

Figure 5.4: (A and B) Representative actograms of a wild-type and a VIP-knockout ($Vip^{-/-}$) mouse kept in LL for 39 d and then constant darkness (DD) for 11 d. Each line shows wheel-running activity in 6-min bins over 48 h with the last 24 h of data replotted on the line below to illustrate free-running circadian periodicity. Cage changes on days 32, 39, and 45 induced locomotor activity, showing that the mice were capable of running on their wheel. (C and D) Time series plots reveal the rapid switch from low-amplitude rhythms in LL to high-amplitude rhythms in DD of the wild-type mouse from A compared with the weak circadian rhythms in LL and DD of the $Vip^{-/-}$ mouse from B. The bar at the bottom of each plot shows the times of lights on (open) and off (shaded). (E) The fold change in the peak-to-trough amplitude of daily locomotion in wild-type animals was reduced dramatically in LL compared with DD, but did not change in $Vip^{-/-}$ mice (mean \pm SEM, n indicates the number of mice; ***P < 0.0005, Student's two-tailed t test).

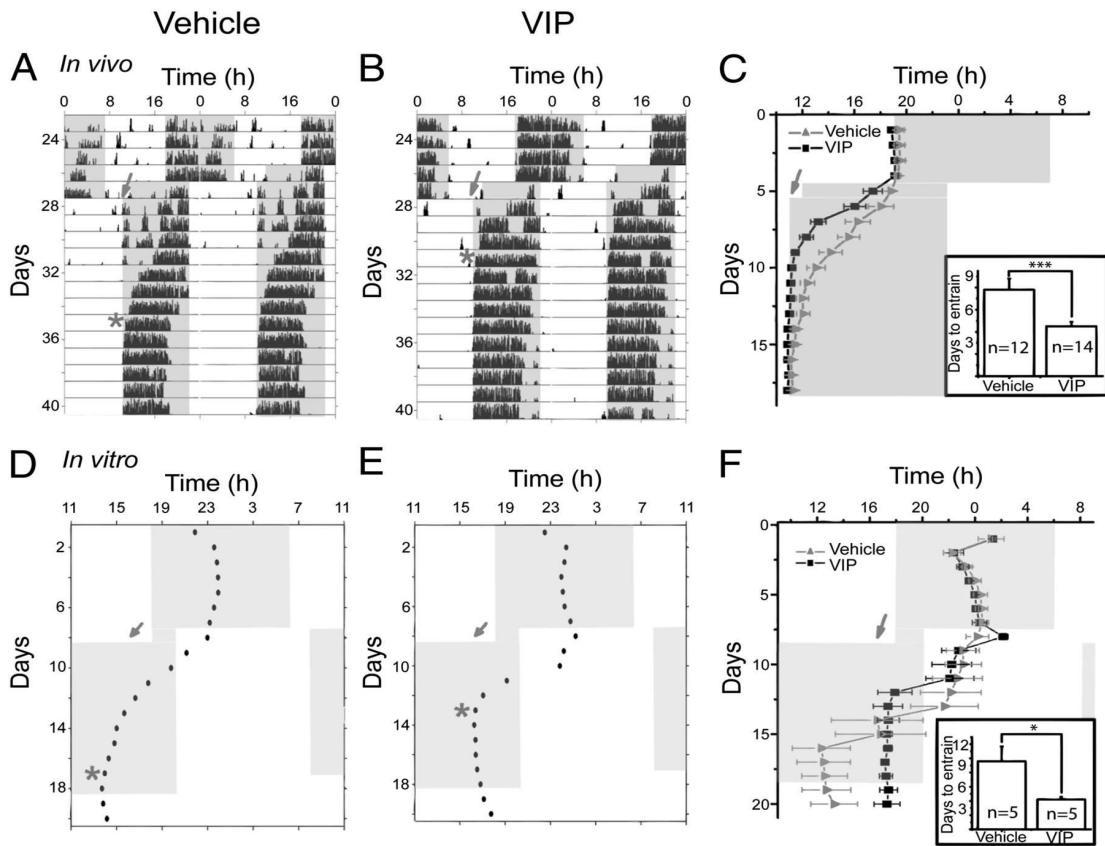


Figure 5.5: VIP accelerates circadian synchronization to an advanced schedule in vivo and in vitro. (A and B) Representative actograms of two mice exposed to an 8-h advance in their light schedule on recording day 27. Mice received either 20 or 200 pmol VIP (B) or vehicle (A) at ZT3 before the shift (shaded arrow) and stably entrained (*) after 4 d (B) or 8 d (A) in the new light schedule. (C) The daily activity onset of all vehicle- or VIP-injected animals (mean \pm SEM) and days required to entrain (mean \pm SEM; Inset).

Figure 5.5: (D and E) Representative actograms of two SCN cultures in a temperature cycle (shaded, 35 °C; open, 36.5 °C). Points show the daily peaks of PER2 expression before and after application of either vehicle (D) or 10 μ M VIP (E) at CT3 (arrow). Note that the vehicle-treated SCN required 8 d to entrain to the new temperature cycle (*) whereas VIP-treated SCN synchronized within 5 d. (F) The daily peak of PER2 expression (mean \pm SEM) of all vehicle- (n = 5) and VIP-treated SCN (n = 5). Note that the vehicle-treated SCN had greater variability in their phases at the end of the temperature cycle. Inset shows that cultures that received VIP entrained significantly faster than controls (mean \pm SEM; *P < 0.05, Student's two-tailed t test).

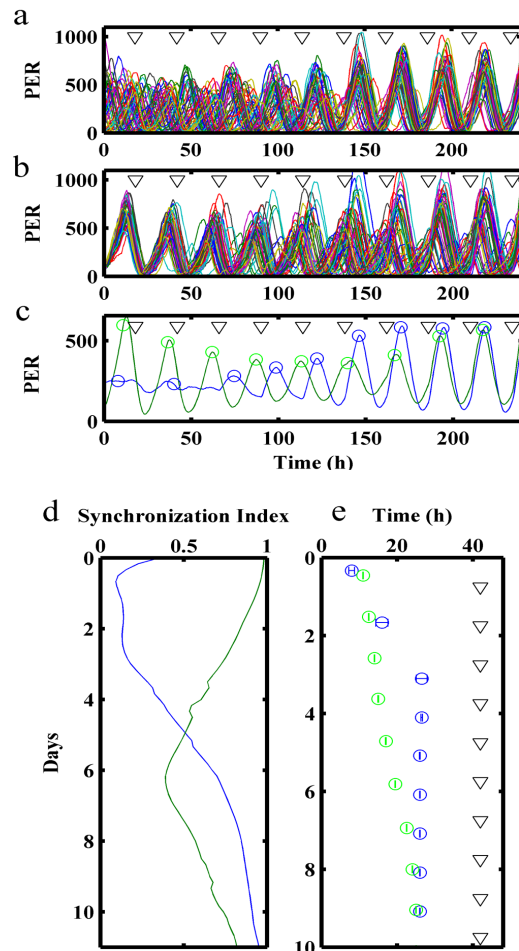


Figure 5.6: A computational model reveals that phase tumbling of circadian oscillators explains VIP-induced desynchrony and predicts that phase tumbling can speed entrainment. (A and B) PER protein levels from stochastic simulations of 49 SCN neurons started with (A) random and (B) synchronized initial phases and then were subjected to a 10-h phase shift via VIP pulses every 24 h (triangles).

Figure 5.6: (C) The mean mRNA level of the 49 cells illustrates the loss of amplitude in the population signal due to loss of synchrony between cells that were initially synchronized (green) or desynchronized (blue). Circles mark PER peaks. (D) Synchronization index and (E) daily peaks of PER (circles, mean \pm SEM) show that desynchronized cells (blue) entrain to VIP (triangles) more quickly than synchronized cells (green).

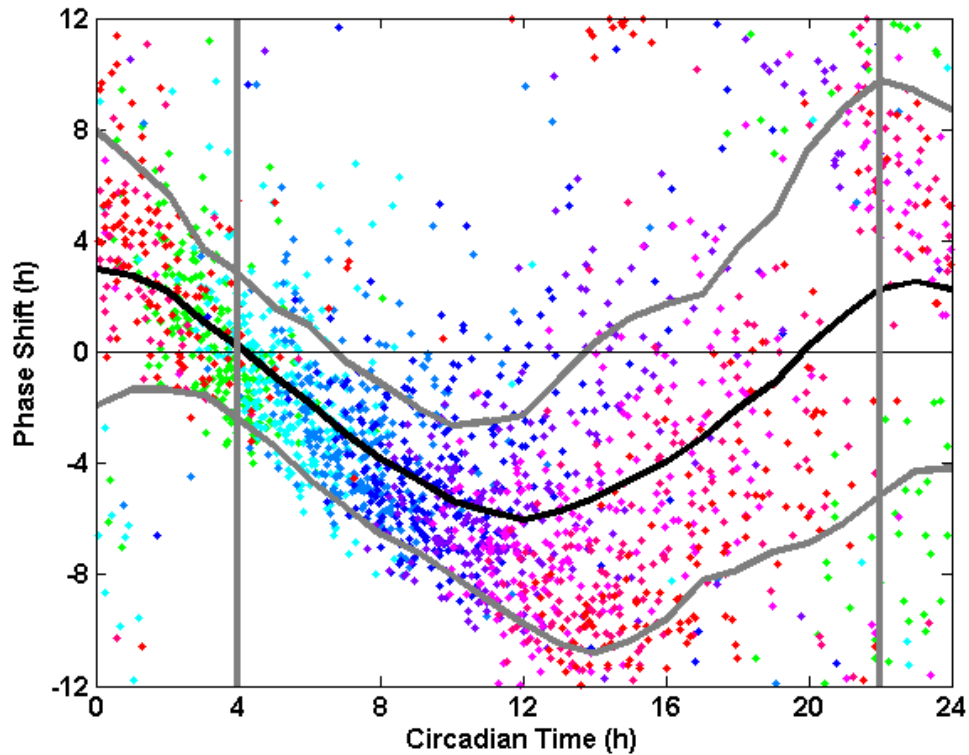


Figure 5.7: Model SCN cells display a time-dependent, stochastic response to VIP stimulation. Consistent with the published phase response curve to VIP, on average (black line), VIP delayed circadian rhythms of individual cells when applied during most of the subjective day (CT5-20) and advanced rhythms when applied during the late subjective night to early morning (CT20-5). The SD of the phase shifts (gray lines) was greatest around CT22 and smallest around CT4 (vertical gray lines).

Figure 5.7: Each point represents the shift of a single, simulated cell in a single VIP application. Each color shows results from five repeated, Monte Carlo trials simulating VIP treatment of 49 uncoupled cells. CT0 was defined as the minimum in Period gene expression as determined by WAVOS, a MATLAB toolkit for wavelet analysis (5). Note that the time of least-phase dispersion (CT4) corresponds to the published time when daily VIP entrains SCN rhythms, but that VIP at any time induces phase dispersion (tumbling). These computational modeling results provide a mechanism by which VIP both reduces synchrony among cells and, when released daily, can entrain SCN rhythms.

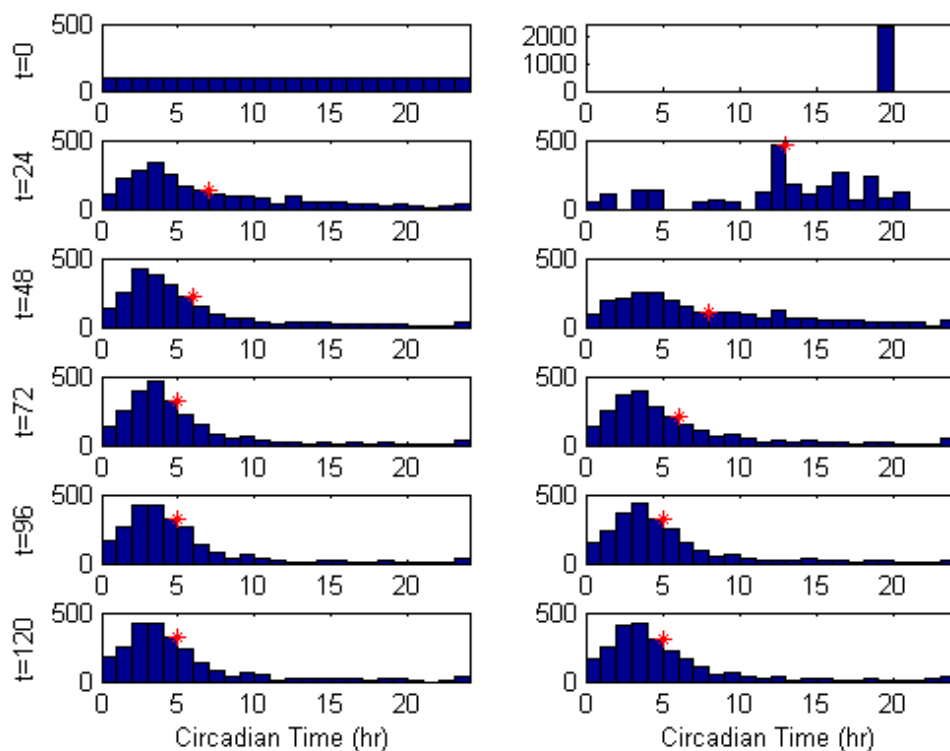


Figure 5.8: A pulse of light was applied to the simulated cells at CT19.5 and every 24 h thereafter. Histograms showing the distribution of cells at 24-h intervals were computed from the PRD. They show rapid convergence to the stable point near CT4 when the initial distribution is desynchronized (Left). When the initial distribution is synchronized (Right), the cells first desynchronize before reentraining and converging to the stable point near CT4. The red asterisks show the mean time of maximal PER expression of each distribution of simulated cells.

Chapter 6

Inference of Functional Network for Synchronization in the SCN

The Suprachiasmatic Nucleus (SCN), a bilateral speck of some 20,000 cells located in the hypothalamus of the mammalian brain, has been demonstrated to control the entrainment of circadian behavior in mammals to light/dark cycles [88]. SCN network dynamics are contingent upon properties of its single cell-autonomous oscillators [68, 10] and the underlying physical connectivity of the network. [12, 62, 108, 8].

Neurons communicate via an electrochemical process, which starts when a neurotransmitter chemical attaches to a neuron's receptor. Information is transmitted by an electrical action potential through the cell's dendrites and axon. When the

signal reaches the end of the axon a neurotransmitter chemical is released, signaling the next neuron. Connectivity in the brain can refer to anatomical connections which can be observed directly[4], statistical dependencies (functional connectivity), or causal interactions (effective connectivity) [98]. Here, we demonstrate a novel method for the inference of functional cellular connections within the SCN based on the maximal information coefficient (MIC) [89].

The maximal information coefficient (MIC) chooses optimal binning for a pair of continuous variables to maximize the mutual information measured between them. Mutual information is particularly well-suited to measuring dependency between neurons in the presence of stochasticity and does not assume a particular function (nonparametric) [17][121]. It has been used to deduce neuron interconnections from neuron firing data [39] [121] [122] and gene regulatory networks from gene-expression microarray data [70].

We inferred functional networks from PER2:LUC recordings of three *in vitro* SCN samples. Movies were produced by recording PER2:LUC bioluminescence in individual cells every hour. Recordings were made during experiments in which the cells were treated for 5 days with tetrodotoxin (TTX) to inhibit inter-cellular coupling and desynchronize their phases while preserving cell-autonomous oscillation [123, 94]. TTX was then washed out, restoring inter-cellular coupling and allowing resynchronization of the cells in the SCN. The information exchanged

between neurons during this 7-10 day resynchronization is quantified by the MIC for all possible pairs of cells. Our results show that the mammalian SCN is functionally connected through a network that displays characteristics of a scale-free small-world topology. The “hubs” of this network are located in the central SCN (Fig. 6.1).

We validate our method by inferring known networks from the results of stochastic simulations using two models of the coupled SCN: a three-state cellular oscillator [44, 93], and an eleven-state cellular oscillator that accounts explicitly for VIP coupling dynamics [2]. As a control, we show that this method is able to differentiate between SCN explants taken from different animals. Finally, we checked that we could re-infer the network from the biological experiment when we implemented it in our model.

The experimental results in this chapter were produced in the lab of Prof. Erik Herzog, Washington University, St. Louis. The theoretical results were obtained in collaboration with John Abel, a UCSB graduate student who is co-advised by Prof. Frank Doyle and Prof. Linda Petzold. A paper describing this work is in preparation.

6.1 Inference Method

While fast electrical connections between neurons may be inferred through methods such as Granger causality or between-sample analysis of connectivity (BSAC) [37], the multielectrode arrays (MEAs) used for data collection are limited in the number of cells that can be monitored and it is difficult to place the electrodes directly on the cells. Here we are interested in using a bioluminescence reporter in an oscillatory system to infer the network. Methods such as delayed mutual information [74] are difficult to use on oscillatory systems due to non-causal correlation. The maximal information coefficient (MIC) [89] provides an efficient pairwise binning of bioluminescence data in phase space, finding the grid that contains the maximum mutual information. Since the selected bins of the two signals are centered on the same time, it avoids registering delayed correlations while, like mutual information, it captures nonlinear relationships between noisy states.

The maximal information coefficient (MIC) [89] is calculated by partitioning a scatter plot of two variables into a grid that maximizes the mutual information. This grid is selected by computing the mutual information between a pair of variables for all grids up to some maximum resolution. The mutual information

I_g for each grid G is

$$I(X; Y) = \int_Y \int_X p(x, y) \log \left(\frac{p(x, y)}{p(x)p(y)} \right) dx dy \quad (6.1)$$

where X and Y are two continuous random variables. The probability of a box in the grid is proportional to the number of points inside it. There are multiple grids with the same x-by-y number of boxes, but with different box size dimensions. The maximum mutual information for each x-by-y grid is selected after normalization to form a matrix m of mutual information values

$$m_{x,y} = \frac{\max(I_g)}{\log \min(x, y)}. \quad (6.2)$$

The MIC is the maximum of $m_{x,y}$ with the number of boxes limited to $xy < B$, where B is a function of sample size, usually $B = n^{0.6}$.

The pairwise MIC provides a continuous measure (0-1) of mutual information. A MIC threshold value must be selected to designate connections. In our validation test, we use the Receiver Operating Characteristic (ROC) curve (Fig. 6.2) to illustrate the performance of the MIC designation as the threshold is varied. It is a plot of the true positive rate (sensitivity) versus the false positive rate (specificity). The area under the ROC curve (AUC) is one measure of performance. An AUC=1.0 indicates perfect detection while an AUC=0.5 indicates an algorithm no better than random chance.

6.2 Validation with Model Circadian Networks

We first validated our network inference method by modeling 100 cells in three different network topology types: random, linear, and Watts-Strogatz [113] using two different cell models: 3-state and 11-state. Inter-cellular coupling was modeled as VIP release from one cell stimulating *Period* transcription in connected cells. In the three-state oscillator, coupling is modeled through algebraic manipulation of *Period* promotion v_s [44, 93]. A cell with index j transcribes mRNA with maximum rate $v_s = v_s^0 + c_j$, where $v_s^0 = 0.82$ is the baseline maximum rate and c_j is the coupling term, which is dependent on the mRNA populations of connected cells. The coupling term is

$$c_j = a \left(\frac{\mathbf{M}_j + w \sum \mathbf{M}_i}{1 + I \times w} - \mathbf{M}_j \right) \quad (6.3)$$

where the coupling strength $a = 2$, M_i is the mRNA population of the connected cell i , I is the total number of connections, and the connection weight $w = 0.0050$. The more detailed eleven-state oscillator explicitly captures VIP and CREB-based *Period* promotion [2]. VIP input to coupled cells was normalized, and cells with no connection received no VIP input. In this model, coupling between neuron 1 and neuron 2 is achieved by VIP mRNA from neuron 1 being directly translated into VIP protein in cell 2, and vice-versa. So that each cell receives the same total VIP input (to keep the model consistent), the VIP input is weighted by the total

number of connections I . The weighting parameter w_i is therefore equal to $1/I$ for each cell (see Table B.1).

We simulated the cells without coupling for five days, allowing them to drift from their initial identical phases to mimic TTX-induced desynchronization. After five days, coupling was restored according to the chosen model network topology and the simulation was continued for another ten days. *Per* mRNA was summed across each one-hour simulation interval to reflect bioluminescence data, with one image taken across each hour. The MIC statistic was calculated as in experiment.

The results in Figure 6.3 show the area under the ROC curve (AUC) versus the average node degree. As the average node degree is increased, the performance of the inference method degrades. This can be attributed to the detection of more false-positive indirect connections. The results shown are all better than random chance (AUC > 0.5).

6.3 Biological Control and Connectivity Threshold

We validated our method with a control using the experimental data: analyzing separate SCN's as if they were one to see if our method would infer false-positive connections between them.

We applied our inference method to bioluminescence traces from the three SCNs, and used a receiver operating characteristic (ROC) curve to determine whether the method can differentiate between biologically distinct SCNs (Fig. 6.4). A “possible positive” was defined to be an inferred connection within the same SCN (Fig. 6.4A), whereas a false positive was a biologically-impossible inferred connection between two different SCNs (Fig. 6.4B). As we only know for certain which connections *cannot* exist, our pseudo-ROC is a comparison of possible positives to false positives (Fig. 6.4D).

To infer the network structure within the SCN, we chose a threshold MIC value, m_c , from the negative control result. Our lowest possible m_c threshold was chosen to be 0.85, as this value has a 0.005 false positive rate, while still capturing the 38,600 strongest bidirectional functional connections within the three SCNs. In order to compare the SCNs and find common structure, we adjusted this threshold to normalize average node degree for each SCN. Because m_c values were raised to normalize node degree, this results in a more conservative estimate of connectivity. For SCNs A, B, and C we set $m_{c,A} = 0.945$, $m_{c,B} = 0.850$, $m_{c,C} = 0.947$, respectively, with an average node degree of 5 for each SCN.

6.4 SCN Network Structure Results

6.4.1 SCN Coupling Displays a Small-World Architecture

The SCN has previously been modeled with a variety of architectures [104, 107, 18, 28]. It is important to characterize the actual functional network structure, as networks of differing architecture display different synchronization and entrainment characteristics, and responses to perturbation. In Table 6.1, we show that networks inferred from our three SCN explants display the characteristics of small-world networks. Small-world networks are commonly found in biological systems, and are defined by the average path length L and clustering coefficient C^Δ , as defined in [113, 78]. A network G is determined to be small world if:

$$L_G \approx L_{random} \text{ and } C_G^\Delta \gg C_{random}^\Delta, \quad (6.4)$$

where the equivalent random graph has an identical number of vertices and edges.

In [56], a “small-world-ness” characteristic is also defined:

$$S^\Delta = \frac{(C_G^\Delta / C_{random}^\Delta)}{(L_G / L_{random})}. \quad (6.5)$$

A network is considered small-world if $S^\Delta > 1$. In Table 6.1, we show that each SCN meets all of the above criteria for small-world architecture, with S^Δ values much greater than one. Values for the random networks are averaged between twenty randomly-generated networks.

Table 6.1: **SCN Network Characteristics**

SCN	n_{cells}	L_{SCN}	L_{rand}	C_{SCN}^Δ	C_{rand}^Δ	S^Δ
A	649	4.63	2.67	0.422	0.027	15.4
B	191	2.88	2.13	0.497	0.098	5.07
C	308	4.00	2.36	0.400	0.058	6.84

Characteristic path length L and clustering coefficient C [113, 78], and S^Δ [56] compared between the inferred network and equivalent randomly-generated networks indicate that the SCN has a small-world topology.

A small-world network is, in addition, determined to be scale-free if the node degree distribution obeys a power law distribution function $P(k)$:

$$P(k) \sim k^{-\gamma}, \quad (6.6)$$

where k is the node degree, for a sufficiently large node count [6]. These networks are free of a characteristic scale. In Fig. 6.5, we show a log-log plot of $P(k)$ vs. k for our three SCN explants, using the above-defined m_c threshold. Fitting to (6.6), we show that for the SCN, on average, $\gamma = 0.89$ ($R^2 = 0.65$). Thus, it appears that the inferred functional SCN networks are approximately scale-free.

Inference of Simulated Networks with Biological Topology

A final validation of our inferred networks is achieved through applying the inferred network topologies to our coupled stochastic models of mammalian circadian rhythm, inferring the networks from simulated data, and computing an ROC curve for the MIC inference method.

In Fig. 6.2, we show that MIC performs moderately well in recapturing simulated SCN networks, with an average area under the ROC curve (AUC) of 0.89 for the three-state model and 0.78 for the eleven-state model. It is important to note that our simulated networks likely do not contain all the physical connections of the SCN explants, as only a two-dimensional layer of cells are observable in bioluminescence experiments.

We inferred the resynchronization network of the SCN using the maximal information coefficient, and found that it met the criteria for being both small-world and scale-free. Previous works have found many neuronal networks to be small-world, and some of these to also be scale-free [32, 16, 99]. Our method does not focus on the phase distribution across the SCN ([36][35][28][81][115][77][63][33]), but instead measures information shared between cells as they resynchronize. We observed more highly connected “hub” cells in the center of the SCN, which is consistent with previous observations of a phase cluster in the core. It would be interesting to examine the functional networks obtained by applying this inference

method to the variety of biological experiments that have been used to observe different phase patterns in the SCN [36][35][28][81][115][77][63][33].

From an information transfer perspective, desynchrony is key to maximizing information transmission in active networks [15]. Baptista et al. [15] investigated optimum network topologies for maximum information transmission over a broad range of coupling strengths and found that a perturbed star topology is optimal for self-excitable channels, while an almost all-to-all connected network is optimal for non-self-excitable channels. A self-excitable channel is responsive (susceptible) to input stimulus or coupling. Baptista et al. asserts that periodic channels are non-self-excitable, but also notes that large amounts of information can be transmitted when bursts are phase synchronous while neuron firing is highly desynchronous. Also, it may be that desynchronization of the SCN allows it to be susceptible to input stimulus such as shifting light schedules [73].

There may be improvements to our analysis that can help eliminate indirect connections and determine communication direction. Multi-point methods, which compare pairwise and triplet mutual information, may help to eliminate indirect connections [19]. A combination of perturbations and temporal resolution could help to uncover causality by determining the order of communication. The transfer entropy which measures the information between the past of one cell and the future of another may be useful in this endeavor [17][39].

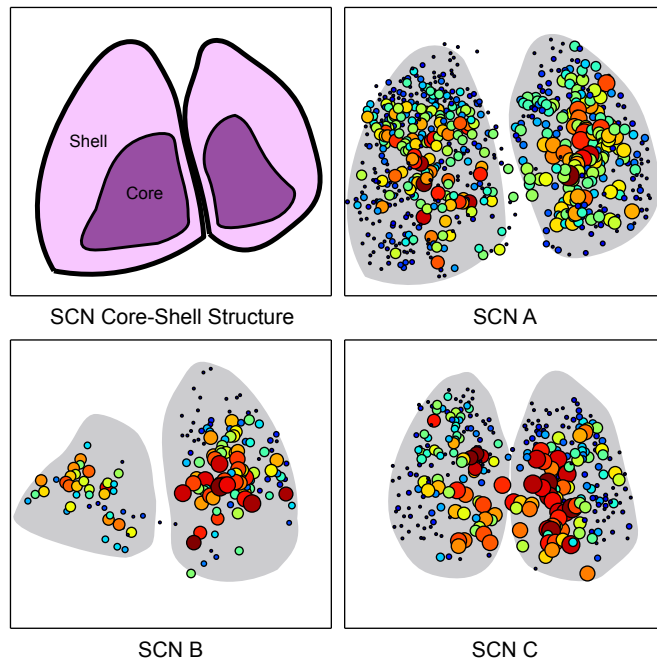


Figure 6.1: **Network inference results for three SCNs.** (A) The SCN displays a core-shell structure. Network inference results (B-D) for three SCNs show that nodes in the central SCN display a higher node degree. Node size in these schematics is proportional to node degree, and color is added for emphasis.

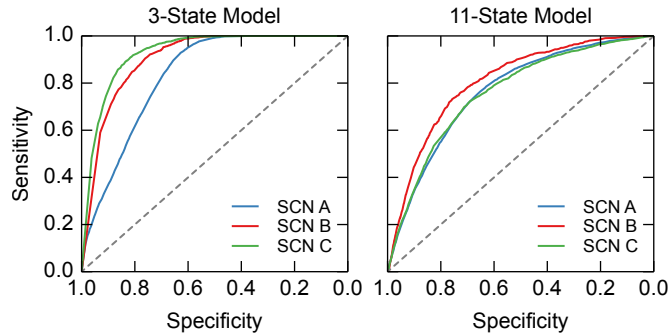


Figure 6.2: **MIC network inference captures simulated networks with topology inferred from experiment.** (A) ROC curves for simulation with the three-state model. Average $AUC = 0.89$. (B) ROC curves for simulation with the eleven-state model. Average $AUC = 0.78$.

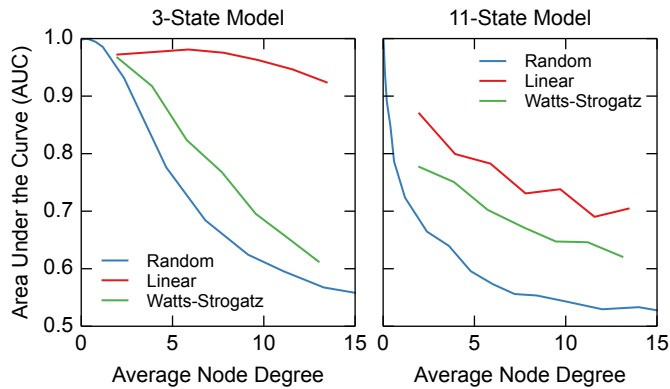


Figure 6.3: **Accuracy of MIC inference method depends on both network topology and average node degree.** Area under the curve is plotted as a function of average node degree for the 3-state model (A) and the 11-state model (B) for these network structures.

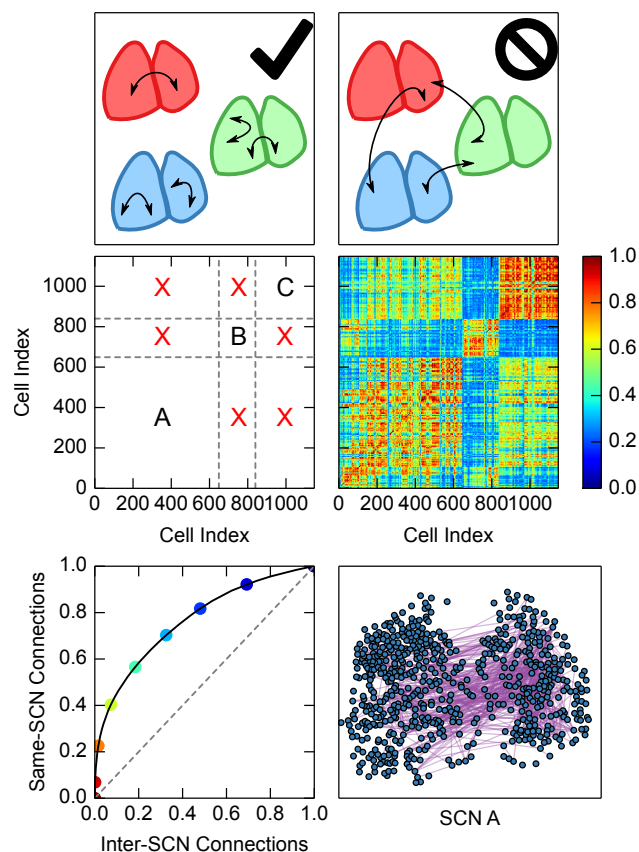


Figure 6.4: MIC correctly distinguishes between SCN samples. (A) For this test, we consider connections within the same SCN to be valid, whether between halves or within a single half. (B) Inter-SCN connections are invalid, as neurons cannot establish connections between biologically separate SCNs. (C) A connectivity plot of MIC values. Higher MIC values (red) indicate stronger phase locking, and synchrony, whereas lower MIC values (blue) indicate little synchrony between cells. Regions A, B, and C represent connections within SCNs A, B, and C, respectively. Regions marked X are inter-SCN (invalid) connections.

Figure 6.4: **(D)** A pseudo-receiver operating characteristic curve for SCN network inference. Colored points along the curve correspond to color in (C) above which connectivity is inferred. As the SCN is not an all-to-all network, we do not expect that all cells should be connected to all others within a single SCN. The first 38,600 connections between SCN cells are inferred with a false positive rate of 0.005 (m_c threshold of 0.85). **(E)** A schematic of the functional network inferred from MIC for SCN A, using $m_{c,A} = 0.98$ for visualization.

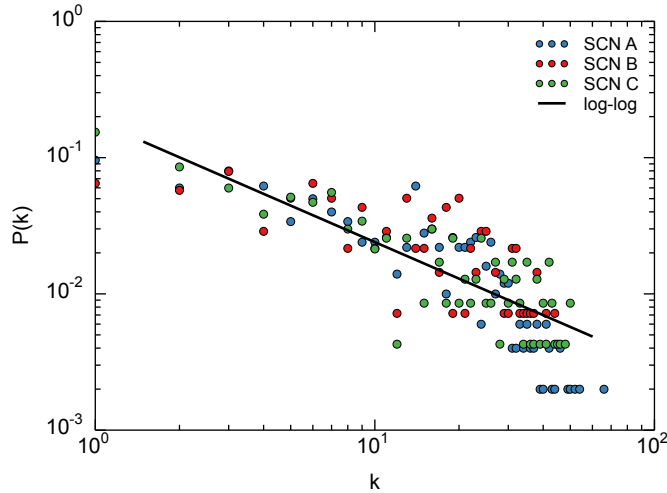


Figure 6.5: **SCN node degree distribution is approximately scale-free.** A network is considered scale-free if node degree distribution obeys a power law fit. Here, we show that this is approximately true for our inferred SCN networks. As the node count is not very high, we see a low R^2 for our fit, as a large number of nodes in each sample is necessary for a smooth exponential fit. $R^2 = 0.65$.

Chapter 7

Conclusions and Future Work

Modeling and simulation, tools of the emerging field of systems biology, may provide answers as to how circadian regulation works and how it can be repaired when broken or altered to improve health. Our work has focused on building a stochastic model of the mammalian circadian system, and examining how noisy stochastic cell oscillators can together form a stable master clock in the SCN.

The oscillations of individual cells and cells in SCN tissue were characterized with a wavelet analysis method, which was used to measure period and phase of the oscillations in noisy non-stationary signals. A comparison of experimental data with stochastic model using wavelet analysis showed a potential explanation for how individual oscillators could be so unstable, yet synchronize in a group: proximity to a bifurcation point in the nonlinear cell model. In the 16-state Leloup

and Goldbeter model this was near a Hopf bifurcation between two oscillation frequencies, rather than near a stable (damped oscillator) solution [18].

We introduced a new theory of how the SCN synchronizes and entrains by phase tumbling when exposed to a shift in light schedule. This theory is based on the probabilistic response of cells with low numbers of molecules, a more faithful representation of their chemistry than a deterministic differential equation model. The randomness of the phase response distribution (PRD) allows the SCN to quickly establish a group of cells at a new light schedule and produce a circadian clock, gaining strength in amplitude as more cells entrain to the new schedule. This work suggests several possible strategies for the reduction of jet-lag involving phase shifts.

Since the response of the SCN system is influenced by the connection topology of its cell network, we next used the measured pairwise maximal information coefficient (MIC) to infer a connection network from experimental data. Several validation tests were done to develop confidence in this method: control comparison of two unconnected SCN samples or modeled SCN networks, as well as inference of the network in models of circadian cells in different types of networks: linear, nearest-neighbor, and random. Since the network inferred from the experimental data was small-world [113], we did a round-trip confirmation that we

could recover the connections from a simulation of the same small-world network of circadian cells.

Future work might address how treating the SCN output as a population distribution may make sense of other observed phenomena such as how exposure to different seasonal day-lengths causes the SCN to respond differently to stimulus. Is the circadian clock adapted differently in animals that live closer to the poles, or in extreme environments such as the bottom of the ocean or in caves where there is no light? Answering these questions may help separate the function of the circadian clock in foraging behavior from its function in internal metabolic processes.

Bibliography

- [1] Danchin A. Important dates 1900 - 1919. Technical report, HKU-Pasteur Research Centre (Paris), 2013.
- [2] J. H. Abel, L. A. Widmer, P. C. St. John, J. Stelling, and F. J. Doyle, III. A Coupled Stochastic Model Explains Differences in Circadian Behavior of Cry1 and Cry2 Knockouts. *ArXiv e-prints*, November 2014.
- [3] Ute Abraham, Adrin E. Granada, Pl O. Westermarck, Markus Heine, Achim Kramer, and Hanspeter Herzl. Coupling governs entrainment range of circadian clocks. *Molecular Systems Biology*, 6:438, Nov 2010.
- [4] Eric E Abrahamson and Robert Y Moore. Suprachiasmatic nucleus in the mouse: retinal innervation, intrinsic organization and efferent projections. *Brain Research*, 916(12):172 – 191, 2001.
- [5] Masashi Akiyama, Yasuko Kouzu, Satomi Takahashi, Hisanori Wakamatsu, Takahiro Moriya, Miyuki Maetani, Shigenori Watanabe, Hajime Tei, Yoshiyuki Sakaki, and Shigenobu Shibata. Inhibition of light- or glutamate-induced mper1 expression represses the phase shifts into the mouse circadian locomotor and suprachiasmatic firing rhythms. *The Journal of Neuroscience*, 19(3):1115–1121, 1999.
- [6] Rka Albert and Albert-Lszl Barabasi. Statistical mechanics of complex networks. *Reviews of Modern Physics*, 74(1):47–, January 2002.
- [7] H Albus, MJ Vansteensel, S Michel, GD Block, and JH Meijer. A GABAergic mechanism is necessary for coupling dissociable ventral and dorsal regional oscillators within the circadian clock. *Current Biology*, 15(10):886–893, May 24 2005.
- [8] Sungwon An, Rich Harang, Kirsten Meeker, Daniel Granados-Fuentes, Connie A. Tsai, Cristina Mazuski, Jihee Kim, Francis J. Doyle, Linda R. Petzold, and Erik D. Herzog. A neuropeptide speeds circadian entrainment by

BIBLIOGRAPHY

- reducing intercellular synchrony. *Proceedings of the National Academy of Sciences*, 2013.
- [9] Sungwon An, Robert P. Irwin, Charles N. Allen, Connie Tsai, and Erik D. Herzog. Vasoactive intestinal polypeptide requires parallel changes in adenylylate cyclase and phospholipase c to entrain circadian rhythms to a predictable phase. *Journal of Neurophysiology*, 105(5):2289–2296, May 2011.
- [10] Bharath Ananthasubramaniam, Erik D Herzog, and Hanspeter Herzel. Timing of Neuropeptide Coupling Determines Synchrony and Entrainment in the Mammalian Circadian Clock. *PLoS Comput. Biol.*, 10(4), 2014.
- [11] Sara J Aton, Christopher S Colwell, Anthony J Harmar, James Waschek, and Erik D Herzog. Vasoactive intestinal polypeptide mediates circadian rhythmicity and synchrony in mammalian clock neurons. *Nature Neuroscience*, 8(4):476–483, April 2005.
- [12] Sara J. Aton and Erik D. Herzog. Come together, right...now: Synchronization of rhythms in a mammalian circadian clock. *Neuron*, 48(4):531–534, November 2005.
- [13] Julie E Baggs, Tom S Price, Luciano DiTacchio, Satchidananda Panda, Garrett A FitzGerald, and John B Hogenesch. Network features of the mammalian circadian clock. *PLoS Biol*, 7(3):e1000052, March 2009.
- [14] Neda Bagheri, Stephanie R. Taylor, Kirsten Meeker, Linda R. Petzold, and Francis J. Doyle. Synchrony and entrainment properties of robust circadian oscillators. *Journal of The Royal Society Interface*, 5(0):S17–S28, August 2008.
- [15] M. S. Baptista, J. X. de Carvalho, and M. S. Hussein. Finding Quasi-Optimal Network Topologies for Information Transmission in Active Networks. *PLOS One*, June 2008.
- [16] Danielle Smith Bassett and Ed Bullmore. Small-world brain networks. *Neuroscientist*, 12(6):512–23, December 2006.
- [17] Demian Battaglia, Annette Witt, Fred Wolf, and Theo Geisel. Dynamic effective connectivity of inter-areal brain circuits. *PLoS Computational Biology*, 8(3):e1002438, 03 2012.

BIBLIOGRAPHY

- [18] Samuel Bernard, Didier Gonze, Branka Cajavec, Hanspeter Herzel, and Achim Kramer. Synchronization-induced rhythmicity of circadian oscillators in the suprachiasmatic nucleus. *PLoS Computational Biology*, 3(4):e68–, April 2007.
- [19] Luis M. A. Bettencourt, Greg J. Stephens, Michael I. Ham, and Guenter W. Gross. Functional structure of cortical neuronal networks grown in vitro. *Physical Review E*, 75:021915, Feb 2007.
- [20] B. Boashash. Estimating and interpreting the instantaneous frequency of a signal. ii. algorithms and applications. *Proceedings of the IEEE*, 80:540–568, 1992.
- [21] Howard C. Breg and Douglas A. Brown, E. Chemotaxis in escherichia coli analysed by three-dimensional tracking. *Nature*, 239(5374):500–504, October 1972.
- [22] Timothy M. Brown, Alun T. Hughes, and Hugh D. Piggins. Gastrin-releasing peptide promotes suprachiasmatic nuclei cellular rhythmicity in the absence of vasoactive intestinal polypeptide-vpac2 receptor signaling. *Journal of Neuroscience*, 25(48):11155–11164, 2005.
- [23] T.M. Brown and H.D. Piggins. Spatiotemporal heterogeneity in the electrical activity of suprachiasmatic nuclei neurons and their response to photoperiod. *Journal of Biological Rhythms*, 24(1):44–54, 2009.
- [24] Ethan D. Buhr, Seung-Hee Yoo, and Joseph S. Takahashi. Temperature as a universal resetting cue for mammalian circadian oscillators. *Science*, 330(6002):379–385, Oct 2010.
- [25] Christopher S. Colwell, Stephan Michel, Jason Itri, Williams Rodriguez, J. Tam, Vincent Lelievre, Zhou Hu, X. Liu, and James A. Waschek. Disrupted circadian rhythms in vip- and phi-deficient mice. *American Journal of Physiology - Regulatory, Integrative and Comparative Physiology*, 285(5):R939–R949, Nov 2003.
- [26] Serge Daan and ColinS. Pittendrigh. A functional analysis of circadian pacemakers in nocturnal rodents. *Journal of Comparative Physiology*, 106(3):253–266, 1976.
- [27] I. Daubechies. Ten lectures on wavelets. *Society for Industrial and Applied Mathematics.*, 1992.

BIBLIOGRAPHY

- [28] Daniel DeWoskin, Weihua Geng, Adam R Stinchcombe, and Daniel B Forger. It is not the parts, but how they interact that determines the behaviour of circadian rhythms across scales and organisms. *Interface Focus*, 4(3):20130076, June 2014.
- [29] Axel C R. Diernfellner, Christina Querfurth, Carlos Salazar, Thomas Hfer, and Michael Brunner. Phosphorylation modulates rapid nucleocytoplasmic shuttling and cytoplasmic accumulation of neurospora clock protein frq on a circadian time scale. *Genes and Development*, 23(18):2192–2200, Sep 2009.
- [30] J. M. Ding, D. Chen, E. T. Weber, L. E. Faiman, M. A. Rea, and M. U. Gillette. Resetting the biological clock: mediation of nocturnal circadian shifts by glutamate and no. *Science*, 266(5191):1713–1717, Dec 1994.
- [31] Jean-Jacques d’Ortous de Mairan. Observation botanique. *Histoire de l’Academie Royale des Sciences*, pages 35–36, 1729.
- [32] Victor M. Eguíluz, Dante R. Chialvo, Guillermo a. Cecchi, Marwan Baliki, and a. Vania Apkarian. Scale-Free Brain Functional Networks. *Phys. Rev. Lett.*, 94(1):018102, January 2005.
- [33] Ryosuke Enoki, Shigeru Kuroda, Daisuke Ono, Mazahir T. Hasan, Tetsuo Ueda, Sato Honma, and Ken-ichi Honma. Topological specificity and hierarchical network of the circadian calcium rhythm in the suprachiasmatic nucleus. *Proc Natl Acad Sci U S A*, 109(52):21498–21503, Dec 2012.
- [34] J. T. Enright. Temporal precision in circadian systems: a reliable neuronal clock from unreliable components? *Science*, 209(4464):1542–1545, Sep 1980.
- [35] Jennifer A. Evans, Tanya L. Leise, Oscar Castanon-Cervantes, and Alec J. Davidson. Dynamic interactions mediated by nonredundant signaling mechanisms couple circadian clock neurons. *Neuron*, 80(4):973–983, Nov 2013.
- [36] Nicholas C. Foley, Tina Y. Tong, Duncan Foley, Joseph Lesauter, David K. Welsh, and Rae Silver. Characterization of orderly spatiotemporal patterns of clock gene activation in mammalian suprachiasmatic nucleus. *Eur J Neurosci*, 33(10):1851–1865, May 2011.
- [37] Jr. Freeman, G.Mark, RebeccaM. Krock, SaraJ. Aton, Paul Thaben, and ErikD. Herzog. Gaba networks destabilize genetic oscillations in the circadian pacemaker. *Neuron*, 78(5):799–806, 2013.

BIBLIOGRAPHY

- [38] Karen L. Gamble, Gregg C. Allen, Tongrong Zhou, and Douglas G. McMahon. Gastrin-releasing peptide mediates light-like resetting of the suprachiasmatic nucleus circadian pacemaker through camp response element-binding protein and per1 activation. *Journal of Neuroscience*, 27(44):12078–12087, Oct 2007.
- [39] Matteo Garofalo, Thierry Nieu, Paolo Massobrio, and Sergio Martinoia. Evaluation of the performance of information theory-based methods and cross-correlation to estimate the functional connectivity in cortical networks. *PLoS ONE*, 4(8):e6482, 08 2009.
- [40] Daniel T. Gillespie. A general method for numerically simulating the stochastic time evolution of coupled chemical reactions. *Journal of Computational Physics*, 22:403–434, 1976.
- [41] Daniel T. Gillespie. The chemical langevin equation. *Journal of Chemical Physics*, 113:297–306, 2000.
- [42] D.T. Gillespie. Exact stochastic simulation of coupled chemical reactions. *Journal of Physical Chemistry*, 81:2340–2361, 1977.
- [43] D. Gonze, S. Bernard, C. Waltermann, A. Kramer, and H. Herzel. Spontaneous synchronization of coupled circadian oscillators. *Biophysical Journal*, 89(1):120–129, July 2005.
- [44] D. Gonze and A. Goldbeter. Circadian rhythms and molecular noise. *Chaos*, 16(2):026110, June 2006.
- [45] D. Gonze, J. Halloy, and A. Goldbeter. Stochastic models for circadian oscillations: Emergence of a biological rhythm. *International Journal Of Quantum Chemistry*, 98(2):228–238, May 2004.
- [46] Maria Luisa Guerriero, Alexandra Pokhilko, Aurora Pias Fernandez, Karen J. Halliday, Andrew J. Millar, and Jane Hillston. Stochastic properties of the plant circadian clock. *Journal of the Royal Society, Interface*, 9(69):744–756, Apr 2012.
- [47] H. Hao, D.E. Zak, T. Sauter, J. Schwaber, and B.A. Ogunnaike. Modeling the VPAC2-activated cAMP/PKA signaling pathway: from receptor to circadian clock gene induction. *Biophysical Journal*, 90(5):1560–1571, Mar 2006.

BIBLIOGRAPHY

- [48] Richard Harang, Kirsten Meeker, Guillaume Bonnet, Francis J. Doyle III, and Linda R. Petzold. Period distribution in mammalian circadian neurons. In *Proceedings Foundations of Systems Biology in Engineering*, 2009.
- [49] Richard E Harang, Guillaume Bonnet, and Linda R Petzold. Wavos: a matlab toolkit for wavelet analysis and visualization of oscillatory systems. *BMC Research Notes*, 5(1):163, 2012.
- [50] Anthony J. Hahner, Hugh M. Marston, Sanbing Shen, Christopher Spratt, Katrine M. West, W John Sheward, Christine F. Morrison, Julia R. Dorin, Hugh D. Piggins, Jean Claude Reubi, John S. Kelly, Elizabeth S. Maywood, and Michael H. Hastings. The *vpac(2)* receptor is essential for circadian function in the mouse suprachiasmatic nuclei. *Cell*, 109(4):497–508, May 2002.
- [51] E. D. Herzog, J. S. Takahashi, and G. D. Block. Clock controls circadian period in isolated suprachiasmatic nucleus neurons. *Nature Neuroscience*, 1(8):708–713, Dec 1998.
- [52] Erik D. Herzog. Neurons and networks in daily rhythms. *Nature Reviews. Neuroscience*, 8(10):790–802, Oct 2007.
- [53] Erik D. Herzog, Sara J. Aton, Rika Numano, Yoshiyuki Sakaki, and Hajime Tei. Temporal precision in the mammalian circadian system: A reliable clock from less reliable neurons. *Journal of Biological Rhythms*, 19:35–46, 2004.
- [54] S. Honma, T. Shirakawa, W. Nakamura, and K. Honma. Synaptic communication of cellular oscillations in the rat suprachiasmatic neurons. *Neuroscience Letters*, 294(2):113–116, Nov 2000.
- [55] Sui Huang. Non-genetic heterogeneity of cells in development: more than just noise. *Development*, 136(23):3853–3862, Dec 2009.
- [56] Mark D Humphries and Kevin Gurney. Network ‘small-world-ness’: a quantitative method for determining canonical network equivalence. *PLoS One*, 3(4):e0002051, January 2008.
- [57] Hsiu-Cheng Hung, Christian Maurer, Daniela Zorn, Wai-Ling Chang, and Frank Weber. Sequential and compartment-specific phosphorylation controls the life cycle of the circadian clock protein. *Journal of Biological Chemistry*, 284(35):23734–23742, Aug 2009.

BIBLIOGRAPHY

- [58] R. V. Jensen. Synchronization of driven nonlinear oscillators. *American Journal of Physics*, 70(6):607–619, 2002.
- [59] M. E. Jewett, R. E. Kronauer, and C. A. Czeisler. Light-induced suppression of endogenous circadian amplitude in humans. *Nature*, 350(6313):59–62, Mar 1991.
- [60] C. H. Johnson. Phase response curves: What can they tell us about circadian clocks ? In T. Hiroshige and K. Honma, editors, *Circadian Clocks from Cell to Human*, chapter Phase response curves: What can they tell us about circadian clocks?, pages 209–249. Hokkaido Univ. Press, Sapporo, 1992.
- [61] Sung-IL Kim, Jaeseung Jeong, Yongho Kwak, Yang In Kim, Seung Hun Jung, and Kyoung J. Lee. Fractal stochastic modeling of spiking activity in suprachiasmatic nucleus neurons. *Journal of Computational Neuroscience*, 19(1):39–51, August 2005.
- [62] Caroline H. Ko, Yujiro R. Yamada, David K. Welsh, Ethan D. Buhr, Andrew C. Liu, Eric E. Zhang, Martin R. Ralph, Steve A. Kay, Daniel B. Forger, and Joseph S. Takahashi. Emergence of Noise-Induced oscillations in the central circadian pacemaker. *PLoS Biol*, 8(10):e1000513, October 2010.
- [63] Satoshi Koinuma, Takeshi Asakawa, Mamoru Nagano, Keiichi Furukawa, Mitsugu Sujino, Koh-Hei Masumoto, Yoshihiro Nakajima, Seiichi Hashimoto, Kazuhiro Yagita, and Yasufumi Shigeyoshi. Regional circadian period difference in the suprachiasmatic nucleus of the mammalian circadian center. *Eur J Neurosci*, 38(6):2832–2841, Sep 2013.
- [64] R. J. Konopka and S. Benzer. Clock mutants of *drosophila melanogaster*. *Proceedings of the National Academy of Sciences of the United States of America*, 68(9):2112–2116, Sep 1971.
- [65] S. Kullback and R. A. Leibler. On information and sufficiency. *The Annals of Mathematical Statistics*, 22(1):79–86, March 1951.
- [66] Jean-Christophe Leloup and Albert Goldbeter. Toward a detailed computational model for the mammalian circadian clock. *Proceedings National Academy of Sciences*, 100(12):7051–7056, 2003.
- [67] Jean-Christophe Leloup and Albert Goldbeter. Modeling the mammalian circadian clock: Sensitivity analysis and multiplicity of oscillatory mechanisms. *Journal of Theoretical Biology*, 230(4):541–562, October 2004.

BIBLIOGRAPHY

- [68] Liu. Transcriptional coactivator pgc-1a integrates the mammalian clock and energy metabolism. *Nature*, 447:477–481, 2007.
- [69] Andrew C. Liu, David K. Welsh, Caroline H. Ko, Hien G. Tran, Eric E. Zhang, Aaron A. Priest, Ethan D. Buhr, Oded Singer, Kirsten Meeker, Inder M. Verma, Francis J. Doyle III, Joseph S. Takahashi, and Steve A. Kay. Intercellular coupling confers robustness against mutations in the scn circadian clock network. *Cell*, 129(3):605–616, May 2007.
- [70] Daniel Marbach, James C Costello, Robert Kuffner, Nicole M Vega, Robert J Prill, Diogo M Camacho, Kyle R Allison, Manolis Kellis, James J Collins, and Gustavo Stolovitzky. Wisdom of crowds for robust gene network inference. *Nat Meth*, 9(8):796–804, August 2012.
- [71] Elizabeth S. Maywood, Akhilesh B. Reddy, Gabriel K.Y. Wong, John S. O’Neill, John A. O’Brien, Douglas G. McMahon, Anthony J. Harmar, Hitoshi Okamura, and Michael H. Hastings. Synchronization and maintenance of timekeeping in suprachiasmatic circadian clock cells by neuropeptidergic signaling. *Current Biology*, 16(6):599–605, March 2006.
- [72] Angela J. McArthur, Andrew N. Coogan, Supaporn Ajpru, David Sugden, Stephany M. Biello, and Hugh D. Piggins. Gastrin-releasing peptide phase-shifts suprachiasmatic nuclei neuronal rhythms in vitro. *The Journal of Neuroscience*, 20(14):5496–5502, 2000.
- [73] Kirsten Meeker, Richard Harang, Alexis B. Webb, David K. Welsh, Francis J. Doyle, Guillaume Bonnet, Erik D. Herzog, and Linda R. Petzold. Wavelet measurement suggests cause of period instability in mammalian circadian neurons. *Journal of Biological Rhythms*, 26(4):353–362, 2011.
- [74] Patrick E Meyer, Frédéric Lafitte, and Gianluca Bontempi. minet: A R/Bioconductor package for inferring large transcriptional networks using mutual information. *BMC Bioinformatics*, 9:461, January 2008.
- [75] Alert Meyer-Spasche and Hugh D. Piggins. Vasoactive intestinal polypeptide phase-advances the rat suprachiasmatic nuclei circadian pacemaker in vitro via protein kinase a and mitogen-activated protein kinase. *Neuroscience Letters*, 358(2):91–94, Mar 2004.
- [76] Alert Meyer-Spasche, Helen E. Reed, and Hugh D. Piggins. Neurotensin phase-shifts the firing rate rhythm of neurons in the rat suprachiasmatic nuclei in vitro. *European Journal of Neuroscience*, 16(2):339–344, Jul 2002.

BIBLIOGRAPHY

- [77] Jihwan Myung, Sungho Hong, Fumiyuki Hatanaka, Yoshihiro Nakajima, Erik De Schutter, and Toru Takumi. Period coding of bmal1 oscillators in the suprachiasmatic nucleus. *J Neurosci*, 32(26):8900–8918, Jun 2012.
- [78] M E Newman, C Moore, and D J Watts. Mean-field solution of the small-world network model. *Phys. Rev. Lett.*, 84(14):3201–4, April 2000.
- [79] Henriette S. Nielsen, Jens Hannibal, and Jan Fahrenkrug. Vasoactive intestinal polypeptide induces per1 and per2 gene expression in the rat suprachiasmatic nucleus late at night. *European Journal of Neuroscience*, 15(3):570–574, Feb 2002.
- [80] Hidenobu Ohta, Shin Yamazaki, and Douglas G. McMahon. Constant light desynchronizes mammalian clock neurons. *Nature Neuroscience*, 8(3):267–269, Mar 2005.
- [81] S. Pauls, N. C. Foley, D. K. Foley, J. LeSauter, M. H. Hastings, E. S. Maywood, and R. Silver. Differential contributions of intra-cellular and inter-cellular mechanisms to the spatial and temporal architecture of the suprachiasmatic nucleus circadian circuitry in wild-type, cryptochrome-null and vasoactive intestinal peptide receptor 2-null mutant mice. *Eur J Neurosci*, 40(3):2528–2540, Aug 2014.
- [82] HD Piggins, MC Antle, and B Rusak. Neuropeptides phase shift the mammalian circadian pacemaker. *Journal of Neuroscience*, 15(8):5612–5622, 1995.
- [83] C. S. Pittendrigh. Circadian systems: entrainment. In J. Aschoff, editor, *Handbook of Behavioral Neurobiology, vol. 4, Biological Rhythms*, chapter Circadian systems: entrainment., pages 95–124. Plenum Press, New York, 1981.
- [84] Tom S. Price, Julie E. Baggs, Anne M. Curtis, Garret A. FitzGerald, and John B. Hogenesch. WAVECLOCK: wavelet analysis of circadian oscillation. *Bioinformatics*, 24(23):2794–2795, December 2008.
- [85] Sandhya R. Pulivarthy, Nobushige Tanaka, David K. Welsh, Luciano De Haro, Inder M. Verma, and Satchidananda Panda. Reciprocity between phase shifts and amplitude changes in the mammalian circadian clock. *Proceedings of the National Academy of Sciences of the United States of America*, 104(51):20356–20361, Dec 2007.

BIBLIOGRAPHY

- [86] H. E. Reed, A. Meyer-Spasche, D. J. Cutler, C. W. Coen, and H. D. Piggins. Vasoactive intestinal polypeptide (vip) phase-shifts the rat suprachiasmatic nucleus clock in vitro. *European Journal of Neuroscience*, 13(4):839–843, Feb 2001.
- [87] Roberto Refinetti. *Circadian Physiology, Second Edition*. CRC Press, 2005.
- [88] Steven M. Reppert and David R. Weaver. Coordination of circadian timing in mammals. *Nature*, 418(6901):935–941, August 2002.
- [89] David N Reshef, Yakir a Reshef, Hilary K Finucane, Sharon R Grossman, Gilean McVean, Peter J Turnbaugh, Eric S Lander, Michael Mitzenmacher, and Pardis C Sabeti. Detecting novel associations in large data sets. *Science (80-.)*, 334(6062):1518–24, December 2011.
- [90] H.J. Romijn, J.F.M. van Uum, J. Emmering, V. Goncharuk, and R.M. Buijs. Colocalization of {VIP} with {AVP} in neurons of the human paraventricular, supraoptic and suprachiasmatic nucleus. *Brain Research*, 832(12):47 – 53, 1999.
- [91] Honma S, Y Katsuno Y FAU Tanahashi, H Tanahashi Y FAU Abe, K Abe H FAU Honma, and Honma K. Circadian rhythms of arginine vasopressin and vasoactive intestinal polypeptide do not depend on cytoarchitecture of dispersed cell culture of rat suprachiasmatic nucleus. *Neuroscience*, 86(0306-4522 (Linking)):967–976, 1998.
- [92] Kevin R. Sanft, Sheng Wu, Min Roh, Jin Fu, Rone Kwei Lim, and Linda R. Petzold. Stochkit2: software for discrete stochastic simulation of biochemical systems with events. *Bioinformatics*, 27(17):2457–2458, Sep 2011.
- [93] Sondra Schroder, Erik D. Herzog, and Istvn Z. Kiss. Transcription-based oscillator model for light-induced splitting as antiphase circadian gene expression in the suprachiasmatic nuclei. *Journal of Biological Rhythms*, 27(1):79–90, 2012.
- [94] W J Schwartz, R a Gross, and M T Morton. The suprachiasmatic nuclei contain a tetrodotoxin-resistant circadian pacemaker. *Proc. Natl. Acad. Sci. U. S. A.*, 84(6):1694–8, March 1987.
- [95] K. Shinohara, S. Honma, Y. Katsuno, H. Abe, and K. Honma. Circadian rhythms in the release of vasoactive intestinal polypeptide and arginine-vasopressin in organotypic slice culture of rat suprachiasmatic nucleus. *Neuroscience Letters*, 170(1):183–186, Mar 1994.

BIBLIOGRAPHY

- [96] K Shinohara, S Honma, Y Katsuno, H Abe, and K Honma. Two distinct oscillators in the rat suprachiasmatic nucleus in vitro. *Proceedings of the National Academy of Sciences*, 92(16):7396–7400, 1995.
- [97] Hao Song, Paul Smolen, Evyatar Av-Ron, Douglas A. Baxter, John H. Byrne, Chuck Yeung, Matthew Shtrahman, and Xiao-lun Wu. Stick-and-diffuse and caged diffusion: A comparison of two models of synaptic vesicle dynamics. *Biophysical Journal*, 92(10):3407–3424, 2007.
- [98] O. Sporns. Brain connectivity. *Scholarpedia*, 2(10):4695, 2007. revision #91083.
- [99] Olaf Sporns and Jonathan D Zwi. The small world of the cerebral cortex. *Neuroinformatics*, 2(2):145–62, January 2004.
- [100] Steven H. Strogatz. From kuramoto to crawford: exploring the onset of synchronization in populations of coupled oscillators. *Physica D: Nonlinear Phenomena*, 143(1-4):1–20, September 2000.
- [101] Stephanie R. Taylor. *Computational Methods for the Analysis of Phase Dynamics in Biological Oscillators*. PhD thesis, University of California, Santa Barbara, 2008.
- [102] S. A. Tischkau, E. A. Gallman, G. F. Buchanan, and M. U. Gillette. Differential camp gating of glutamatergic signaling regulates long-term state changes in the suprachiasmatic circadian clock. *Journal of Neuroscience*, 20(20):7830–7837, Oct 2000.
- [103] Shelley A. Tischkau, E. Todd Weber, Sabra M. Abbott, Jennifer W. Mitchell, and Martha U. Gillette. Circadian clock-controlled regulation of cgmp-protein kinase g in the nocturnal domain. *The Journal of Neuroscience*, 23(20):7543–7550, 2003.
- [104] T. L. To, M. A. Henson, E. D. Herzog, and F. J. Doyle. A molecular model for intercellular synchronization in the mammalian circadian clock. *Biophysical Journal*, 92(11):3792–3803, June 2007.
- [105] Hideki Ukai, Tetsuya J. Kobayashi, Mamoru Nagano, Koh-hei Masumoto, Mitsugu Sujino, Takao Kondo, Kazuhiro Yagita, Yasufumi Shigeyoshi, and Hiroki R. Ueda. Melanopsin-dependent photo-perturbation reveals desynchronization underlying the singularity of mammalian circadian clocks. *Nature Cell Biology*, 9(11):1327–1334, Nov 2007.

BIBLIOGRAPHY

- [106] Henk Tjebbe vanderLeest, Jos H. T. Rohling, Stephan Michel, and Johanna H. Meijer. Phase shifting capacity of the circadian pacemaker determined by the scn neuronal network organization. *PLoS ONE*, 4(3):e4976, 03 2009.
- [107] Christina Vasalou, ED Herzog, and MA Henson. Small-world network models of intercellular coupling predict enhanced synchronization in the suprachiasmatic nucleus. *J. Biol. Rhythms*, 24(3):1–19, 2009.
- [108] Christina Vasalou, Erik D Herzog, and Michael A Henson. Multicellular model for intercellular synchronization in circadian neural networks. *Biophys. J.*, 101(1):12–20, July 2011.
- [109] M. H. Vitaterna, D. P. King, A. M. Chang, J. M. Kornhauser, P. L. Lowrey, J. D. McDonald, W. F. Dove, L. H. Pinto, F. W. Turek, and J. S. Takahashi. Mutagenesis and mapping of a mouse gene, clock, essential for circadian behavior. *Science*, 264(5159):719–725, Apr 1994.
- [110] Martha Hotz Vitaterna, Caroline H. Ko, Anne-Marie Chang, Ethan D. Buhr, Ethan M. Fruechte, Andrew Schook, Marina P. Antoch, Fred W. Turek, and Joseph S. Takahashi. The mouse clock mutation reduces circadian pacemaker amplitude and enhances efficacy of resetting stimuli and phase-response curve amplitude. *Proceedings of the National Academy of Sciences of the United States of America*, 103(24):9327–9332, Jun 2006.
- [111] Andrew M. Vosko, Analyne Schroeder, Dawn H. Loh, and Christopher S. Colwell. Vasoactive intestinal peptide and the mammalian circadian system. *General and Comparative Endocrinology*, 152(2-3):165–175, 2007.
- [112] K. Watanabe, J. Vanecek, and S. Yamaoka. In vitro entrainment of the circadian rhythm of vasopressin-releasing cells in suprachiasmatic nucleus by vasoactive intestinal polypeptide. *Brain Research*, 877(2):361–366, Sep 2000.
- [113] D. J. Watts and S. H. Strogatz. Collective dynamics of ‘small-world’ networks. *Nature*, 393(6684):440–442, Jun 1998.
- [114] Alexis B. Webb, Nikhil Angelo, James E. Huettner, and Erik D. Herzog. Intrinsic, nondeterministic circadian rhythm generation in identified mammalian neurons. *Proceedings of the National Academy of Sciences*, 106(38):16493–16498, 2009.

BIBLIOGRAPHY

- [115] Alexis B. Webb, Stephanie R. Taylor, Kurt A. Thoroughman, Francis J Doyle, 3rd, and Erik D. Herzog. Weakly circadian cells improve resynchrony. *PLoS Comput Biol*, 8(11):e1002787, 2012.
- [116] D. K. Welsh, D. E. Logothetis, M. Meister, and S. M. Reppert. Individual neurons dissociated from rat suprachiasmatic nucleus express independently phased circadian firing rhythms. *Neuron*, 14(4):697–706, Apr 1995.
- [117] David K. Welsh, Takato Imaizumi, Steve A. Kay, and Michael W. Young. Real-Time reporting of Circadian-Regulated gene expression by luciferase imaging in plants and mammalian cells. *Methods in Enzymology*, Volume 393:269–288, 2005.
- [118] David K Welsh, Joseph S Takahashi, and Steve A Kay. Suprachiasmatic nucleus: cell autonomy and network properties. *Annual Review of Physiology*, 72:551–577, March 2010. PMID: 20148688.
- [119] A. T. Winfree. Unclocklike behaviour of biological clocks. *Nature*, 253(5490):315–319, Jan 1975.
- [120] Kyung-Chul Woo, Tae-Don Kim, Kyung-Ha Lee, Do-Yeon Kim, Wanil Kim, Kyung-Yeol Lee, and Kyong-Tai Kim. Mouse period 2 mrna circadian oscillation is modulated by ptb-mediated rhythmic mrna degradation. *Nucleic Acids Research*, 37(1):26–37, Jan 2009.
- [121] Jinghua Xu, Zeng rong Liu, Ren Liu, and Qing fei Yang. Information transmission in human cerebral cortex. *Physica D: Nonlinear Phenomena*, 106(34):363 – 374, 1997.
- [122] Satoshi Yamada, Kenji Matsumoto, Michio Nakashima, and Satoru Shiono. Information theoretic analysis of action potential trains ii. analysis of correlation among n neurons to deduce connection structure. *Journal of Neuroscience Methods*, 66(1):35 – 45, 1996.
- [123] Shun Yamaguchi, Hiromi Isejima, Takuya Matsuo, Ryusuke Okura, Kazuhiro Yagita, Masaki Kobayashi, and Hitoshi Okamura. Synchronization of cellular clocks in the suprachiasmatic nucleus. *Science*, 302(5649):1408–1412, 2003.
- [124] Seung-Hee Yoo, Shin Yamazaki, Phillip L. Lowrey, Kazuhiro Shimomura, Caroline H. Ko, Ethan D. Buhr, Sandra M. Siepka, Hee-Kyung Hong, Won Jun Oh, Ook Joon Yoo, Michael Menaker, and Joseph S. Takahashi.

BIBLIOGRAPHY

Inaugural article: *Period2::luciferase* real-time reporting of circadian dynamics reveals persistent circadian oscillations in mouse peripheral tissues. *Proceedings of the National Academy of Sciences*, 101(15):5339–5346, 2004.

Appendix A

Leloup and Goldbeter 16-state Discrete Stochastic Model

This model is the discrete stochastic version of model in [104], which, in turn, is constructed from Leloup and Goldbeter’s [66] 16-state mammalian model. In Table A.1 we list the reactions involved in a single cell. To convert molar concentrations in the deterministic model to populations (number of each chemical species) requires converting the concentration to units of molecules per liter then multiplying by a cell volume V . The scaling constant Ω is given by

$$\Omega = N_A[\text{molecules/liter}] \times V[\text{liters}] \quad (\text{A.1})$$

where Avogadro’s number $N_A = 6.022 \times 10^{23}$. For $\Omega = 600$ used in this model

$$1\text{nM} \times \Omega = 1\text{nM} \times \frac{1\text{M}}{10^9\text{nM}} \times 6.022 \times 10^{23} \text{molecules/liter} \times V\text{liters}. \quad (\text{A.2})$$

Solving for V gives a volume of $V = 1.7e^{-15}$ liters.

Table A.1: Reactions of discrete stochastic model based on 16 state Leloup & Goldbeter model with added CREB equation

	Reaction	Probability of reaction	Transitions
0	$G \rightarrow G + M_P$	$w_0 = (\nu_{sP}\Omega) \frac{B_N^n}{(K_{AP}\Omega)^n + B_N^n}$	$M_P \rightarrow M_P + 1$
1	$M_P \rightarrow$	$w_1 = (\nu_{mP}\Omega) \frac{M_P}{(K_{mP}\Omega) + M_P}$	$M_P \rightarrow M_P - 1$

Appendix A. *Leloup and Goldbeter 16-state Discrete Stochastic Model*

Table A.1 Continued: Reactions of discrete stochastic model based on 16 state Leloup & Goldbeter model with added CREB equation

Reaction	Probability of reaction	Transitions
2 $M_P \rightarrow$	$w_2 = k_{dmp}M_P$	$M_P \rightarrow M_P - 1$
3 $G \rightarrow G + M_C$	$w_3 = (\nu_{sC}\Omega) \frac{B_N^n}{(K_{AC}\Omega)^n + B_N^n}$	$M_C \rightarrow M_C + 1$
4 $M_C \rightarrow$	$w_4 = (\nu_{mC}\Omega) \frac{M_C}{(K_{mC}\Omega) + M_C}$	$M_C \rightarrow M_C - 1$
5 $M_C \rightarrow$	$w_5 = k_{dmc}M_C$	$M_C \rightarrow M_C - 1$
6 $G \rightarrow G + M_B$	$w_6 = (\nu_{sB}\Omega) \frac{(K_{IB}\Omega)^m}{(K_{IB}\Omega)^m + B_N^m}$	$M_B \rightarrow M_B + 1$
7 $M_B \rightarrow$	$w_7 = (\nu_{mb}\Omega) \frac{M_B}{(K_{mB}\Omega) + M_B}$	$M_B \rightarrow M_B - 1$
8 $M_B \rightarrow$	$w_8 = k_{dmb}M_B$	$M_B \rightarrow M_B - 1$
9 $M_P \rightarrow P_C$	$w_9 = k_{sp}M_P$	$P_C \rightarrow P_C + 1$
10 $P_C \rightarrow P_{CP}$	$w_{10} = (V_{1P}\Omega) \frac{P_C}{(K_p\Omega) + P_C}$	$P_C \rightarrow P_C - 1$
		$P_{CP} \rightarrow P_{CP} + 1$
11 $P_{CP} \rightarrow P_C$	$w_{11} = (V_{2P}\Omega) \frac{P_{CP}}{(K_{dp}\Omega) + P_{CP}}$	$P_C \rightarrow P_C + 1$
		$P_{CP} \rightarrow P_{CP} - 1$
12 $PC_C \rightarrow P_C + C_C$	$w_{12} = k_4PC_C$	$P_C \rightarrow P_C + 1$
		$C_C \rightarrow C_C + 1$
		$PC_C \rightarrow PC_C - 1$
13 $P_C + C_C \rightarrow PC_C$	$w_{13} = \left(\frac{k_3}{\Omega}\right)P_C C_C$	$P_C \rightarrow P_C - 1$
		$C_C \rightarrow C_C - 1$
		$PC_C \rightarrow PC_C + 1$
14 $P_C \rightarrow$	$w_{14} = k_{dn}P_C$	$P_C \rightarrow P_C - 1$
15 $M_C \rightarrow C_C$	$w_{15} = k_{sC}M_C$	$C_C \rightarrow C_C + 1$
16 $C_C \rightarrow C_{CP}$	$w_{16} = (V_{1C}\Omega) \frac{C_C}{(K_p\Omega) + C_C}$	$C_C \rightarrow C_C - 1$
		$C_{CP} \rightarrow C_{CP} + 1$
17 $C_{CP} \rightarrow C_C$	$w_{17} = (V_{2C}\Omega) \frac{C_{CP}}{(K_{dp}\Omega) + C_{CP}}$	$C_C \rightarrow C_C + 1$
		$C_{CP} \rightarrow C_{CP} - 1$
18 $C_C \rightarrow$	$w_{18} = k_{dnc}C_C$	$C_C \rightarrow C_C - 1$
19 $P_{CP} \rightarrow$	$w_{19} = (\nu_{dPC}\Omega) \frac{P_{CP}}{(K_d\Omega) + P_{CP}}$	$P_{CP} \rightarrow P_{CP} - 1$
20 $P_{CP} \rightarrow$	$w_{20} = k_{dn}P_{CP}$	$P_{CP} \rightarrow P_{CP} - 1$
21 $C_{CP} \rightarrow$	$w_{21} = (\nu_{dCC}\Omega) \frac{C_{CP}}{(K_d\Omega) + C_{CP}}$	$C_{CP} \rightarrow C_{CP} - 1$
22 $C_{CP} \rightarrow$	$w_{22} = k_{dn}C_{CP}$	$C_{CP} \rightarrow C_{CP} - 1$
23 $PC_C \rightarrow PC_{CP}$	$w_{23} = (V_{1PC}\Omega) \frac{PC_C}{(K_p\Omega) + PC_C}$	$PC_C \rightarrow PC_C - 1,$
		$PC_{CP} \rightarrow PC_{CP} + 1$

Appendix A. *Leloup and Goldbeter 16-state Discrete Stochastic Model*

Table A.1 Continued: Reactions of discrete stochastic model based on 16 state Leloup & Goldbeter model with added CREB equation

Reaction	Probability of reaction	Transitions
24 $PC_{CP} \rightarrow PC_C$	$w_{24} = (V_{2PC}\Omega) \frac{PC_{CP}}{(K_{dp}\Omega) + PC_{CP}}$	$PC_C \rightarrow PC_C + 1,$ $PC_{CP} \rightarrow PC_{CP} - 1$
25 $PC_N \rightarrow PC_C$	$w_{25} = k_2 PC_N$	$PC_C \rightarrow PC_C + 1,$ $PC_N \rightarrow PC_N - 1$
26 $PC_C \rightarrow PC_N$	$w_{26} = k_1 PC_C$	$PC_C \rightarrow PC_C - 1,$ $PC_N \rightarrow PC_N + 1$
27 $PC_C \rightarrow$	$w_{27} = k_{dn} PC_C$	$PC_C \rightarrow PC_C - 1$
28 $PC_N \rightarrow PC_{NP}$	$w_{28} = (V_{3PC}\Omega) \frac{PC_N}{(K_p\Omega) + PC_N}$	$PC_N \rightarrow PC_N - 1,$ $PC_{NP} \rightarrow PC_{NP} + 1$
29 $PC_{NP} \rightarrow PC_N$	$w_{29} = (V_{4PC}\Omega) \frac{PC_{NP}}{(K_{dp}\Omega) + PC_{NP}}$	$PC_N \rightarrow PC_N + 1,$ $PC_{NP} \rightarrow PC_{NP} - 1$
30 $PC_N + B_N \rightarrow I_N$	$w_{30} = \left(\frac{k_7}{\Omega}\right) PC_N B_N$	$PC_N \rightarrow PC_N - 1,$ $B_N \rightarrow B_N - 1$ $I_N \rightarrow I_N + 1$
31 $I_N \rightarrow PC_N + B_N$	$w_{31} = k_8 I_N$	$PC_N \rightarrow PC_N + 1,$ $B_N \rightarrow B_N + 1$ $I_N \rightarrow I_N - 1$
32 $PC_N \rightarrow$	$w_{32} = k_{dn} PC_N$	$PC_N \rightarrow PC_N - 1$
33 $PC_{CP} \rightarrow$	$w_{33} = (V_{dPCC}\Omega) \frac{PC_{CP}}{(K_d\Omega) + PC_{CP}}$	$PC_{CP} \rightarrow PC_{CP} - 1$
34 $PC_{CP} \rightarrow$	$w_{34} = k_{dn} PC_{CP}$	$PC_{CP} \rightarrow PC_{CP} - 1$
35 $PC_{NP} \rightarrow$	$w_{35} = (V_{dPCN}\Omega) \frac{PC_{NP}}{(K_d\Omega) + PC_{NP}}$	$PC_{NP} \rightarrow PC_{NP} - 1$
36 $PC_{NP} \rightarrow$	$w_{36} = k_{dn} PC_{NP}$	$PC_{NP} \rightarrow PC_{NP} - 1$
37 $M_B \rightarrow B_C$	$w_{37} = k_{sB} M_B$	$B_C \rightarrow B_C + 1$
38 $B_C \rightarrow B_{CP}$	$w_{38} = (V_{1B}\Omega) \frac{B_C}{(K_p\Omega) + B_C}$	$B_C \rightarrow B_C - 1,$ $B_{CP} \rightarrow B_{CP} + 1$
39 $B_{CP} \rightarrow B_C$	$w_{39} = (V_{2B}\Omega) \frac{B_{CP}}{(K_{dp}\Omega) + B_{CP}}$	$B_C \rightarrow B_C + 1,$ $B_{CP} \rightarrow B_{CP} - 1$
40 $B_C \rightarrow B_N$	$w_{40} = k_5 B_C$	$B_C \rightarrow B_C - 1$ $B_N \rightarrow B_N + 1$
41 $B_N \rightarrow B_C$	$w_{41} = k_6 B_N$	$B_C \rightarrow B_C + 1$ $B_N \rightarrow B_N - 1$

Appendix A. *Leloup and Goldbeter 16-state Discrete Stochastic Model*

Table A.1 Continued: Reactions of discrete stochastic model based on 16 state Leloup & Goldbeter model with added CREB equation

Reaction	Probability of reaction	Transitions
42 $B_C \rightarrow$	$w_{42} = k_{dn} B_C$	$B_C \rightarrow B_C - 1$
43 $B_{CP} \rightarrow$	$w_{43} = (V_{dBC} \Omega) \frac{B_{CP}}{(K_d \Omega) + B_{CP}}$	$B_{CP} \rightarrow B_{CP} - 1$
44 $B_{CP} \rightarrow$	$w_{44} = k_{dn} B_{CP}$	$B_{CP} \rightarrow B_{CP} - 1$
45 $B_N \rightarrow B_{NP}$	$w_{45} = (V_{3B} \Omega) \frac{B_N}{(K_p \Omega) + B_N}$	$B_N \rightarrow B_N - 1$ $B_{NP} \rightarrow B_{NP} + 1$
46 $B_{NP} \rightarrow B_N$	$w_{46} = (V_{4B} \Omega) \frac{B_{NP}}{(K_{dp} \Omega) + B_{NP}}$	$B_N \rightarrow B_N + 1$ $B_{NP} \rightarrow B_{NP} - 1$
47 $B_N \rightarrow$	$w_{47} = k_{dn} B_N$	$B_N \rightarrow B_N - 1$
48 $B_{NP} \rightarrow$	$w_{48} = (V_{dBN} \Omega) \frac{B_{NP}}{(K_d \Omega) + B_{NP}}$	$B_{NP} \rightarrow B_{NP} - 1$
49 $B_{NP} \rightarrow$	$w_{49} = k_{dn} B_{NP}$	$B_{NP} \rightarrow B_{NP} - 1$
50 $I_N \rightarrow$	$w_{50} = (V_{dIN} \Omega) \frac{I_N}{(K_d \Omega) + I_N}$	$I_N \rightarrow I_N - 1$
51 $I_N \rightarrow$	$w_{51} = k_{dn} I_N$	$I_N \rightarrow I_N - 1$
52 $CB^* \rightarrow$	$w_{52} = \Omega \left(\frac{\nu_P}{CB_T} \right) \left[\left(\frac{\nu_K}{\nu_P} \right) \frac{\Omega - CB^*}{K_1 + (\Omega - CB^*)} \right]$	$CB^* \rightarrow CB^* + 1$
53 $CB^* \rightarrow$	$w_{53} = \Omega \left(\frac{\nu_P}{CB_T} \right) \frac{CB^*}{K_2 + CB^*}$	$CB^* \rightarrow CB^* - 1$

Table A.2: Parameter values for 16 state molecular clock model

<i>Parameter</i>	<i>Value</i>
$k_1(1/h)$	0.4
$k_2(1/h)$	0.2
$k_3(1/(nM \cdot h))$	0.4
$k_4(1/h)$	0.2
$k_5(1/h)$	0.4
$k_6(1/h)$	0.4
$k_7(1/(nM \cdot h))$	0.5
$k_8(1/h)$	0.1
$k_{AP}(nM)$	0.7
$k_{AC}(nM)$	0.6

Table A.2 Continued: Parameter values for 16 state molecular clock model

<i>Parameter</i>	<i>Value</i>
$k_{IB}(nM)$	2.2
$k_{dmb}(1/h)$	0.01
$k_{dmc}(1/h)$	0.01
$k_{dmp}(1/h)$	0.01
$k_{dn}(1/h)$	0.01
$k_{dnc}(1/h)$	0.12
$K_d(nM)$	0.3
$K_{dp}(nM)$	0.1
$K_p(nM)$	0.1
$K_{mB}(nM)$	0.4
$K_{mC}(nM)$	0.4
$K_{mP}(nM)$	0.31
$k_{sB}(1/h)$	0.12
$k_{sC}(1/h)$	1.6
$k_{sP}(1/h)$	0.6
m	2
n	4
$V_{1B}(nM/h)$	0.5
$V_{1C}(nM/h)$	0.6
$V_{1P}(nM/h)$	0.4
$V_{1PC}(nM/h)$	0.4
$V_{2B}(nM/h)$	0.1
$V_{2C}(nM/h)$	0.1
$V_{2P}(nM/h)$	0.3
$V_{2PC}(nM/h)$	0.1
$V_{3B}(nM/h)$	0.5
$V_{3PC}(nM/h)$	0.4
$V_{4B}(nM/h)$	0.2
$V_{4PC}(nM/h)$	0.1
$V_{phos}(nM/h)$	0.4
$\nu_{dBC}(nM/h)$	0.5
$\nu_{dBN}(nM/h)$	0.6
$\nu_{dCC}(nM/h)$	0.7
$\nu_{dIN}(nM/h)$	0.8

Table A.2 Continued: Parameter values for 16 state molecular clock model

<i>Parameter</i>	<i>Value</i>
$\nu_{dPC}(nM/h)$	0.7
$\nu_{dPCC}(nM/h)$	0.7
$\nu_{dPCN}(nM/h)$	0.7
$\nu_{mB}(nM/h)$	0.8
$\nu_{mC}(nM/h)$	1.0
$\nu_{mP}(nM/h)$	1.1
$\nu_{sB}(nM/h)$	1.0
$\nu_{sC}(nM/h)$	1.1
$\nu_{sP0}(nM/h)$	1.1
Ω	90
a	10.0
b	4.0
N	49
$K_D(nM)$	2.0
$k(1/h)$	10.0
$\nu_0(nM/h)$	0.5
$\nu_1(nM/h)$	5.0
$V_{MK}(nM/h)$	8.0
$K_a(nM)$	2.5
$CB_T(nM)$	1.0
$K_C(nM)$	0.3
$C_T(nM)$	0.4

Appendix B

11-state Circadian Model

The model described in this Appendix was developed by John Abel and submitted for publication [2]. For stochastic simulation using this model, $\Omega = 400$ was used to convert biomolecule concentrations to populations.

Table B.1: Ordinary differential equations comprising the 11-state circadian model.

State Variable	Symbol	Model Equation
<i>Per</i> mRNA	p	$\frac{d\mathbf{p}}{dt} = \frac{v_{1pp}\mathbf{CREB} + v_{2pr}}{K_{1p} + \mathbf{C1P} + \mathbf{C2P}} - \frac{v_{3p}\mathbf{P}}{K_{2dp} + \mathbf{p}}$
<i>Cry1</i> mRNA	c1	$\frac{d\mathbf{c1}}{dt} = \frac{v_{4c1r}}{K_{3c} + \mathbf{C1P} + \mathbf{C2P}} - \frac{v_{5c1}\mathbf{c1}}{K_{4dc} + \mathbf{c1}}$
<i>Cry2</i> mRNA	c2	$\frac{d\mathbf{c2}}{dt} = \frac{v_{6c2r}}{K_{3c} + \mathbf{C1P} + \mathbf{C2P}} - \frac{v_{7c2}\mathbf{c2}}{K_{4dc} + \mathbf{c2}}$
<i>VIP</i> mRNA	vip	$\frac{d\mathbf{vip}}{dt} = \frac{v_{8vr}}{K_{5v} + \mathbf{C1P} + \mathbf{C2P}} - \frac{v_{9v}\mathbf{vip}}{K_{6dv} + \mathbf{vip}}$
PER Protein	PER	$\begin{aligned} \frac{d\mathbf{P}}{dt} = & k_{1p}\mathbf{P} - \frac{v_{10P}\mathbf{P}}{K_{8dP} + \mathbf{P}} - v_{11aCP}\mathbf{P} \times \mathbf{C1} \\ & - v_{11aCP}\mathbf{P} \times \mathbf{C2} + v_{12dCP}\mathbf{C1P} + v_{12dCP}\mathbf{C2P} \end{aligned}$

Appendix B. 11-state Circadian Model

Table B.1 Continued: Ordinary differential equations comprising the 11-state circadian model.

State Variable	Symbol	Model Equation
CRY1 Protein	C1	$\frac{d\mathbf{C1}}{dt} = k_{2c}\mathbf{c1} - \frac{v_{13C1}\mathbf{C1}}{K_{9dC} + \mathbf{C1}} - v_{11aCP}\mathbf{P} \times \mathbf{C1}$ $+ v_{12dCP}\mathbf{C1P}$
CRY2 Protein	C2	$\frac{d\mathbf{C2}}{dt} = k_{2c}\mathbf{c2} - \frac{v_{14C2}\mathbf{C2}}{K_{9dC} + \mathbf{C2}} - v_{11aCP}\mathbf{P} \times \mathbf{C2}$ $+ v_{12dCP}\mathbf{C2P}$
VIP Protein	VIP	$\frac{d\mathbf{VIP}_j}{dt} = k_{3v} \sum_i^I w_i \mathbf{vip}_i - v_{15V}\mathbf{VIP}_j$
CRY1-PER Dimer	C1P	$\frac{d\mathbf{C1P}}{dt} = v_{11aCP}\mathbf{P} \times \mathbf{C1} - v_{12dCP}\mathbf{C1P}$ $- \frac{v_{16C1P}\mathbf{C1P}}{K_{10dCn} + \mathbf{C1P} + \mathbf{C2P}}$
CRY2-PER Dimer	C2P	$\frac{d\mathbf{C2P}}{dt} = v_{11aCP}\mathbf{P} \times \mathbf{C2} - v_{12dCP}\mathbf{C2P}$ $- \frac{v_{17C2P}\mathbf{C2P}}{K_{10dCn} + \mathbf{C1P} + \mathbf{C2P}}$
CREB Protein	CREB	$\frac{d\mathbf{CREB}}{dt} = \frac{v_{18V}\mathbf{VIP}}{K_{11V} + \mathbf{VIP}} - \frac{v_{19CR}\mathbf{CREB}}{K_{12dCR} + \mathbf{CREB}}$

Table B.2: Parameter descriptions for the 11-state circadian ODE model.

Parameter	Description	Value	Units
v_{1pp}	CREB-induced <i>Per</i> mRNA promotion	0.235	[-]/hr
v_{2pr}	<i>Per</i> mRNA transcription	0.415	[-] ² /hr
v_{3p}	<i>Per</i> mRNA degradation	0.478	[-]/hr
v_{4c1r}	<i>Cry1</i> mRNA transcription	0.350	[-] ² /hr
v_{5c1}	<i>Cry1</i> mRNA degradation	1.44	[-]/hr
v_{6c2r}	<i>Cry2</i> mRNA transcription	0.124	[-]/hr
v_{7c2}	<i>Cry2</i> mRNA degradation	2.28	[-]/hr
v_{8vr}	<i>VIP</i> mRNA transcription	0.291	[-] ² /hr
v_{9v}	<i>VIP</i> mRNA degradation	1.35	[-]/hr
v_{10P}	PER protein degradation	13.0	[-]/hr
v_{11aCP}	PER-CRY dimer formation	0.493	([-] × hr) ⁻¹
v_{12dcp}	PER-CRY dimer dissociation	0.00380	1/hr
v_{13C1}	CRY1 protein degradation	4.12	[-]/hr
v_{14C2}	CRY2 protein degradation	0.0862	[-]/hr
v_{15V}	VIP protein degradation	0.723	1/hr
v_{16C1P}	PER-CRY1 dimer degradation	0.0306	[-]/hr
v_{17C2P}	PER-CRY2 dimer degradation	0.840	[-]/hr
v_{18V}	CREB activation by VIP receptors	0.789	[-]/hr
v_{19CR}	CREB deactivation	1.27	[-]/hr
k_{1p}	PER translation	7.51	1/hr
k_{2c}	CRY translation	0.572	1/hr
k_{3v}	VIP translation	5.50	1/hr
K_{1p}	<i>Per</i> transcription constant	0.264	[-]
K_{2dp}	<i>Per</i> degradation constant	0.00795	[-]
K_{3c}	<i>Cry</i> transcription constant	0.156	[-]
K_{4dc}	<i>Cry</i> degradation constant	1.94	[-]
K_{5v}	<i>VIP</i> transcription constant	0.115	[-]
K_{6dv}	<i>VIP</i> degradation constant	0.110	[-]
K_{7dP}	PER protein degradation constant	0.0372	[-]
K_{8dC}	CRY protein degradation constant	4.23	[-]
K_{9dCn}	PER-CRY dimer degradation constant	0.0455	[-]
K_{10V}	CREB protein activation constant	1.46	[-]
K_{11CR}	CREB protein deactivation constant	1.01	[-]